Tectonic history of the Kyrgyz South Tien Shan (Atbashi-Inylchek) suture zone: The role of inherited structures during deformation-propagation

S. Glorie,[1] J. De Grave,[1] M. M. Buslov,[2] F. I. Zhimulev,[2] D. F. Stockli,[3] V. Y. Batalev,[4] A. Izmer,[5] P. Van den haute,[1] F. Vanhaecke,[5] and M. A. Elburg[1,6]

Received 19 May 2011; revised 22 August 2011; accepted 14 October 2011; published 29 December 2011.

[1] Multimethod chronology was applied on intrusives bordering the Kyrgyz South Tien Shan suture (STSs) to decipher the timing of (1) formation and amalgamation of the suturing units and (2) intracontinental deformation that built the bordering mountain ranges. Zircon U/Pb data indicate similarities between the Tien Shan and Tarim Precambrian crust. Caledonian (~440–410 Ma) and Hercynian (~310–280 Ma) zircon U/Pb ages were found at the edge of the STSs, related to subduction and closure of the Turkestan Ocean and the formation of the suture itself. Permian-Triassic (~280–210 Ma) titanite fission track and zircon (U-Th)/He data record the first signs of exhumation when the STSs evolved into a shear zone and the adjacent Tarim basin started to subside. Low-temperature thermochronological (apatite fission track, zircon and apatite (U-Th)/He) analyses reveal three distinct cooling phases, becoming younger toward the STSs center: (1) Jurassic-Cretaceous cooling ages provide evidence that a Mesozoic South Tien Shan orogen formed as a response to the Cimmerian orogeny; (2) Early Paleogene (~60–45 Ma) data indicate a renewed pulse of STSs reactivation during the Early Cenozoic; (3) Neogene ages constrain the onset of the modern Tien Shan mountain building to the Late Oligocene (~30–25 Ma), which intensified during the Miocene (~10–8 Ma) and Pliocene (~3–2 Ma). The Cenozoic signals may reflect renewed responses to collisions at the southern Eurasian border (i.e., the Kohistan-Dras and India-Eurasia collisions). This progressive rejuvenation of the STSs demonstrates that deformation has not migrated steadily into the forelands, but was focused on pre-existing basement structures.

Citation: Glorie, S., J. De Grave, M. M. Buslov, F. I. Zhimulev, D. F. Stockli, V. Y. Batalev, A. Izmer, P. Van den haute, F. Vanhaecke, and M. A. Elburg (2011), Tectonic history of the Kyrgyz South Tien Shan (Atbashi-Inylchek) suture zone: The role of inherited structures during deformation-propagation, *Tectonics*, *30*, TC6016, doi:10.1029/2011TC002949.

1. Introduction and Geological Setting

[2] The ancestral Central Asian Orogenic Belt (CAOB) [e.g., *Jahn*, 2004] or Altaids [*Şengör et al.*, 1993] represents the world's largest accretionary orogen, pinched in between the rigid Tarim block on its southern border and the Siberian craton in the north. Its basement records an amalgamation of various tectonic units which were assembled during Paleozoic accretion and collision events, related to the closure of the Paleo-Asian Ocean (PAO) [*Windley et al.*, 2007]. During the Meso-Cenozoic, closure of the Tethyan Oceans and ensuing convergence and collision of "Tethyan tectonic units" introduced major stress and deformation in the CAOB basement [e.g., *De Grave et al.*, 2007]. In this context, a significant portion of stress was partitioned further into the continental interior along pre-existing zones of weakened continental lithosphere. These often correspond to inherited structures such as suture zones which remain as relics of earlier accretion and collision events associated with the amalgamation of the ancestral CAOB [*Molnar and Tapponnier*, 1975; *Abdrakhmatov et al.*, 1996; *Windley et al.*, 2007]. Hence, as a consequence of the large-scale reactivation of basement structures, intracontinental orogens were built superimposed on the basement structure of the CAOB [*Avouac et al.*, 1993; *Allen and Vincent*, 1997; *Buslov et al.*, 2007; *De Grave et al.*, 2007; *Yin*, 2010]. Since

[1]Department of Geology and Soil Science, Ghent University, Ghent, Belgium.
[2]Institute of Geology and Mineralogy, Siberian Branch of the Russian Academy of Sciences, Novosibirsk, Russia.
[3]Department of Geology, University of Kansas, Lawrence, Kansas, USA.
[4]International Geodynamics Research Centre, Bishkek, Kyrgyzstan.
[5]Department of Analytical Chemistry, Ghent University, Ghent, Belgium.
[6]School of Geological Sciences, University of KwaZulu-Natal, Durban, South Africa.

0278-7407/11/2011TC002949

inherited structures generally record the first signs of deformation, understanding the structural fabric is the key to unravel intracontinental deformation processes as a whole [*Hendrix and Davis*, 2001; *Jolivet et al.*, 2010].

[3] The Tien Shan, located at the southwestern margin of the CAOB, is one of the world's best expressed intracontinental orogens. This more than 2500 km long mountain belt with peaks exceeding 7000 m in altitude, extends from West to East through the Republics of Uzbekistan, Kazakhstan, Tajikistan, Kyrgyzstan and China (Xinjiang province) (Figure 1). The Tien Shan can be subdivided into four tectonic domains: Northern (NTS), Northeastern, (NETS), Middle (MTS) and Southern (STS) Tien Shan [*Konopelko et al.*, 2007; *Biske and Seltmann*, 2010; *Seltmann et al.*, 2011] (Figure 1). In the Kyrgyz Tien Shan, only parts of the NTS, MTS and STS are present. In further discussion, we refer to Caledonian and Hercynian granitoids when they were emplaced in the Kyrgyz Tien Shan basement during respectively Early Paleozoic (Cambrian-Silurian) and Late Paleozoic (Carboniferous-Permian) tectonic events [e.g., *Konopelko et al.*, 2007, 2008; *Seltmann et al.*, 2011]. The NTS is built up by Precambrian micro-continental fragments related to the Paleo-Kazakhstan continent [*Windley et al.*, 2007; *Biske and Seltmann*, 2010]. This tectonic terrane contains numerous Caledonian granitoids that were intruded during subduction and closure of the Terskey Ocean, a branch of the PAO at that time [*Konopelko et al.*, 2008; *Qian et al.*, 2009; *Glorie et al.*, 2010; *Ren et al.*, 2011; *Seltmann et al.*, 2011]. The MTS, also known as the Yili block in China [e.g., *Gao et al.*, 2009; *Qian et al.*, 2009], represents a Precambrian micro-continent with inferred Tarim-affinity [*Kröner et al.*, 2009; *Biske and Seltmann*, 2010; *Kheraskova et al.*, 2010]. It docked to the NTS after closure of the Terskey Ocean and the formation of the Nikolaev Line. The MTS is therefore considered as the Caledonian passive margin of Paleo-Kazakhstan [*Gao et al.*, 2009; *Biske and Seltmann*, 2010; *Ren et al.*, 2011]. South of the MTS, the STS represents a Late Paleozoic accretionary complex at the active margin of the Tarim microcontinent, which attached to Paleo-Kazakhstan during Hercynian times [*Bazhenov et al.*, 1993; *Konopelko et al.*, 2007; *Seltmann et al.*, 2011]. The NETS is entirely located in China and therefore, beyond the scope of this paper. A more detailed description of the Paleozoic Tien Shan subdivision and tectonic history can be found, for example, in the works by *Allen et al.* [1993], *Gao et al.* [1998, 2009], *Glorie et al.* [2010], *Kheraskova et al.* [2010], *Xiao et al.* [2010], *Seltmann et al.* [2011], and *De Grave et al.* [2011a].

[4] After the Hercynian Tien Shan orogeny, the construction of the ancestral Tien Shan was completed. The assembly and subsequent break-up of Pangea in the Late Paleozoic–Early Mesozoic induced large-scale rotations in the Tien Shan paleo-orogen and associated shear movements along its Paleozoic sutures [*Bazhenov et al.*, 1993, 1999; *Van der Voo et al.*, 2006]. During this period, the Karatau/Talas-Ferghana Fault (TFF; Figure 1) became active as such a large-scale shear zone and played an important role in the post-orogenic deformation of the ancestral Tien Shan [*Burtman et al.*, 1996; *Allen et al.*, 2001; *Alexeiev et al.*, 2009]. Deformation caused by Meso-Cenozoic collisions at the distant southern Eurasian margin, propagated into the Tien Shan realm induced several reactivation episodes [*Hendrix et al.*, 1994; *Yin et al.*, 1998; *Schwab et al.*, 2004; *Sobel et al.*, 2006a, 2006b; *De Grave et al.*, 2007; *Kapp et al.*, 2007; *Glorie et al.*, 2010]. As a consequence, the Tien Shan experienced renewed deformation and became uplifted. Furthermore in this framework, the Paleozoic tectonic units were displaced for more than 200 km along the reactivated TFF [*Burtman et al.*, 1996]. Hence, the resulting present-day NE–SW striking Tien Shan mountainous topography reflects both its inherited Paleozoic basement architecture and its Meso-Cenozoic reactivation history [*Allen and Vincent*, 1997; *Poupinet et al.*, 2002; *Buslov et al.*, 2007]. Geodetic studies estimate the modern shortening rate across the entire Tien Shan as ~20 (±3) mm/yr [*Abdrakhmatov et al.*, 1996; *Reigber et al.*, 2001], testifying that Cenozoic Tien Shan tectonics remain very active.

[5] The ophiolite-bearing South Tien Shan suture (STSs) is an important example of a reactivated basement structure in the Tien Shan edifice. This suture, also known as the Turkestan suture [*Bazhenov et al.*, 1993] or South Central Tianshan suture [*Gao et al.*, 1998; 2009] is thought to be a relic of the Turkestan Ocean, a remnant PAO branch, which closed during the Late Paleozoic convergence between the Tarim and Paleo-Kazakhstan continents. During and after this collision, Hercynian granitoids were emplaced into the entire Tien Shan basement, across the terrane boundaries [*Zonenshain et al.*, 1990; *Gao and Klemd*, 2003; *Konopelko et al.*, 2007; *B. Wang et al.*, 2009; *Xiao et al.*, 2010; *Seltmann et al.*, 2011].

[6] In recent years, a large data set of zircon U/Pb ages was collected on these syn- and post-collisional granitoids along the suture zone. Based on these data, the closure of the Turkestan Ocean was dated around 320–300 Ma and its associated post-collisional magmatism around 290–275 Ma [*Konopelko et al.*, 2007, 2009; *Gao et al.*, 2009, 2011; *B. Wang et al.*, 2009; *Biske and Seltmann*, 2010; *Hegner et al.*, 2010; *Su et al.*, 2010; *Seltmann et al.*, 2011].

[7] In comparison with its Paleozoic evolution, relatively little is known about the subsequent Meso-Cenozoic tectonic history of the STSs. For the Chinese Tien Shan, thermochronological studies on granitoids and sedimentary rocks revealed distinct preserved Mesozoic and Cenozoic reactivation phases along the sutures that border the tectonic terranes of the Tien Shan, such as the STSs [*Dumitru et al.*, 2001; *Q. Wang et al.*, 2009; *Jolivet et al.*, 2010]. However, the adjacent Kyrgyz STSs segments, locally known as the Atbashi and Inylchek segments [e.g., *Solomovich*, 2007; *Biske and Seltmann*, 2010], are poorly studied and thermochronological data is lacking. In this study, we therefore targeted granitoid intrusions along these Kyrgyz STSs segments for a multichronological study, aiming to (1) obtain more detailed information on the timing of the accretionary tectonics of the ancestral Kyrgyz Tien Shan, (2) reconstruct the thermotectonic history of the Kyrgyz STSs in relation to the different reactivation events it went through and (3) enhance our present understanding of intracontinental deformation in the Tien Shan orogen in general. This multichronological approach combines several temperature-sensitive dating methods on single rock samples. In order to produce an internally consistent data set and to have high-temperature benchmarks for subsequent thermal history modeling, we also determined the zircon U/Pb ages of the studied granitoids. This information allows us to understand

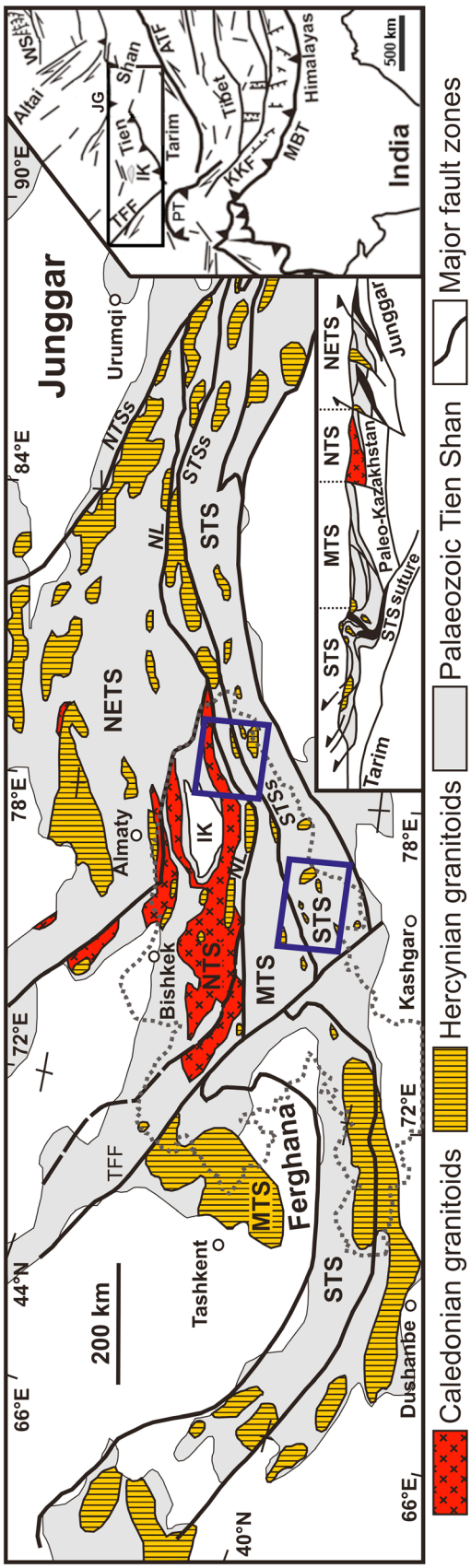

Figure 1. Schematic map of the Tien Shan with indication of its Caledonian and Hercynian intrusive complexes [after *Zhang et al.*, 2004; *Konopelko et al.*, 2007; *Gao et al.*, 2009, 2011; *Seltmann et al.*, 2011]. Based on its main structural fabric, the Tien Shan can be subdivided into the Northeastern (NETS), Northern (NTS), Middle (MTS) and Southern Tien Shan (STS). These tectonic units are separated by ophiolitic suture zones such as the Nikolaev Line (NL) and the South Tien Shan suture (STSs). The blue boxes along the STSs refer to the sample location maps in Figure 2. Inset 1: Location map of the Tien Shan within Central Asia. ATF = Altyn-Tagh Fault, IK = Issyk-Kul lake, JG = Junggar basin, MBT = Main Boundary Thrust, KKF = Karakoram Fault, PT = Pamir Thrust, TFF = Talas Ferghana Fault, WS = West-Sayan Fault. Inset 2: Schematic SW-NE cross-section through the Tien Shan [after *Biske and Seltmann*, 2010].

how the ancestral Tien Shan was assembled and how its composing tectonic terranes are related, which is crucially important to unravel the neotectonic evolution of the Tien Shan.

2. Sample Sites Along the Kyrgyz Segments (Atbashi-Inylchek) of the STSs

[8] Sampling occurred along several mainly N-S profiles across the NE–SW trending Atbashi (western branch) and Inylchek (eastern branch) segments of the STS suture (Figure 2). A table with sample details can be found in Table S1 in the auxiliary material.[1] The Atbashi segment is characterized by the gneiss-schist-quartzite Atbashi metamorphic complex, which includes ophiolite lenses and high-pressure–low-temperature (HP-LT) metamorphosed rocks (eclogite, blueschist) [*Solomovich*, 2007; *Simonov et al.*, 2008]. Ophiolites are represented by a serpentinitic mélange, including dunites, pyroxenites and gabbroids, covered by basalts and cherts [*Alekseev et al.*, 2007]. The HP-LT rocks show also traces of retrograde metamorphism. Ar/Ar dating on co-existing phengite and glaucophane reveals a 327–324 Ma crystallization age for the Atbashi HP-LT rocks [*Simonov et al.*, 2008]. More recent Sm/Nd and Ar/Ar ages on the eclogite mineral assemblage indicated that HP metamorphism, exhumation and exposure of the HP mélange occurred from ~320–300 Ma [*Hegner et al.*, 2010]. Their Chinese counterparts were extensively dated with Sm/Nd, Rb/Sr and Ar/Ar methods yielding ages of 345–310 Ma [*Gao and Klemd*, 2003; *Klemd et al.*, 2005; *Su et al.*, 2010; *Wang et al.*, 2010].

[9] Along both the north and south sides of the Atbashi metamorphic complex, relative small granitoid outcrops occur (Figure 2). These were the main targets for our study across the Atbashi STSs segment. The MTS granitoids at the northern edge were mapped as rocks belonging to the Early Permian Ashukultor subvolcanic complex by *Zhukov et al.* [2008]. The Kembel massif represents a small stock in this complex composed of porphyritic granites and monzodiorites, from which a small vertical profile (samples AI-69, 71, 72, 73; ~300 m elevation difference) was sampled. South of the Atbashi metamorphic complex, several Early Permian granitoids crop out. These are post-collisional granitoids that were emplaced in the aftermath of the Hercynian STS orogeny (Figure 2). We collected five samples from the Mudryum (AI-82), Kok-Kiya (AI-79), Tashrabat (AI-75, 77) and Torugart (AI-74) massifs [*Konopelko et al.*, 2007; *Zhukov et al.*, 2008] (Figure 2). According to *Konopelko et al.* [2007], these leucogranitic intrusives are mainly metaluminous to slightly peraluminous with a pronounced A_2-type affinity. Furthermore, two samples were taken from the southern section of the gneissic Atbashi metamorphic complex (AI-62, Kyr-21) and one from a tonalite (AI-60) intrusion within the ophiolitic mélange (Figure 2).

[10] In addition, we analyzed one detrital sample (Kyr-31) from the Paleogene *Kokturpak Formation*, just north of the Atbashi metamorphic complex. This Formation is well-known for the occurrence of breccias and conglomerates with a carbonate cement and paleosols, with the latter indicating a Paleogene episode of tectonic quiescence and peneplanation in the Tien Shan [*Cobbold et al.*, 1994].

[11] The Inylchek segment of the STSs is characterized by the calc-alkaline Terektinsky complex (Figure 2). This granitoid body intruded the MTS basement and was thrust south onto the alluvial deposits of the Inylchek river during Meso-Cenozoic events. The river marks the STSs in this region. *Grishenko* [1985] subdivided the Terektinsky complex into (1) the Kaindybulak complex, a presumably Silurian intrusion, and (2) the Terektinsky complex s.s. with presumed Carboniferous age. *Konopelko et al.* [2009] however found no age difference between both complexes. The latter authors sampled both intrusive complexes and found only one Early Permian zircon U/Pb age population (295–292 Ma). We sampled a vertical profile (AI-11, 12, 13, 14; ~500 m elevation difference) crossing both Terektinsky intrusive complexes, close to Inylchek village (Figure 2). These sample sites form part of a larger traverse across the Inylchek STSs segment, extending further south across the Tashkoro (AI-16) massif. This massif forms part of the peraluminous leucogranitic [*Solomovich*, 2007] STS stocks which also show A_2-type affinity based on their Ga/Al ratios [*Konopelko et al.*, 2009]. To the north, our sampled profile crosscuts the MTS intrusives. Samples AI-15 and AI-20 were taken from the Precambrian Sary-Dzhaz granitoids, north of the STSs [*Zhukov et al.*, 2008] (Figure 2). Further west, two additional samples were taken in the MTS (Akshairak Range). Sample AI-31 comes from a felsic tuff, centrally located in the MTS, while AI-29 was sampled in migmatites just north of the STSs (Figure 2).

3. Analytical Procedures

[12] In total, twenty-one basement samples and one additional conglomerate sample were analyzed in this study using the zircon U/Pb (ZUPb), titanite fission track (TFT), zircon (U-Th)/He (ZHe), apatite fission track (AFT) and apatite (U-Th)/He (AHe) dating methods. On most samples a combination of dating methods was used (Figure 2). Apatite, zircon and titanite were separated from the rocks, using conventional techniques. Subsequently, euhedral/subhedral inclusion-free grains from these separates were prepared to be dated with the aforementioned methods. Combining these dating methods, which are sensitive in distinct temperature (T) intervals, allows us to constrain and interpret the thermotectonic history of the Kyrgyz STSs.

3.1. Zircon U/Pb (ZUPb) Dating

[13] Zircon separates from a total of seventeen granitoid and gneissic samples across the Kyrgyz STSs were embedded and polished for LA-ICP-(SF)-MS (Laser Ablation-Inductively Coupled Plasma-(Sector Field)-Mass Spectrometry) U/Pb dating. Using this technique, the zircon crystallization ages (closure-T of ~800–1000°C) of the sampled intrusives were determined [*Cherniak and Watson*, 2003]. The U/Pb analyses were carried out at the LA-ICP-(SF)-MS facility of the Department of Analytical Chemistry at Ghent University, using identical analytical procedures as described by *Glorie et al.* [2011]. The internal structure of the zircon crystals was investigated and mapped by cathodoluminescence (CL) imaging, using a JEOL JSM-6400 SEM (Scanning Electron Microscope). Reference zircon GJ-1 [*Jackson*

[1]Auxiliary materials are available in the HTML. doi:10.1029/2011TC002949.

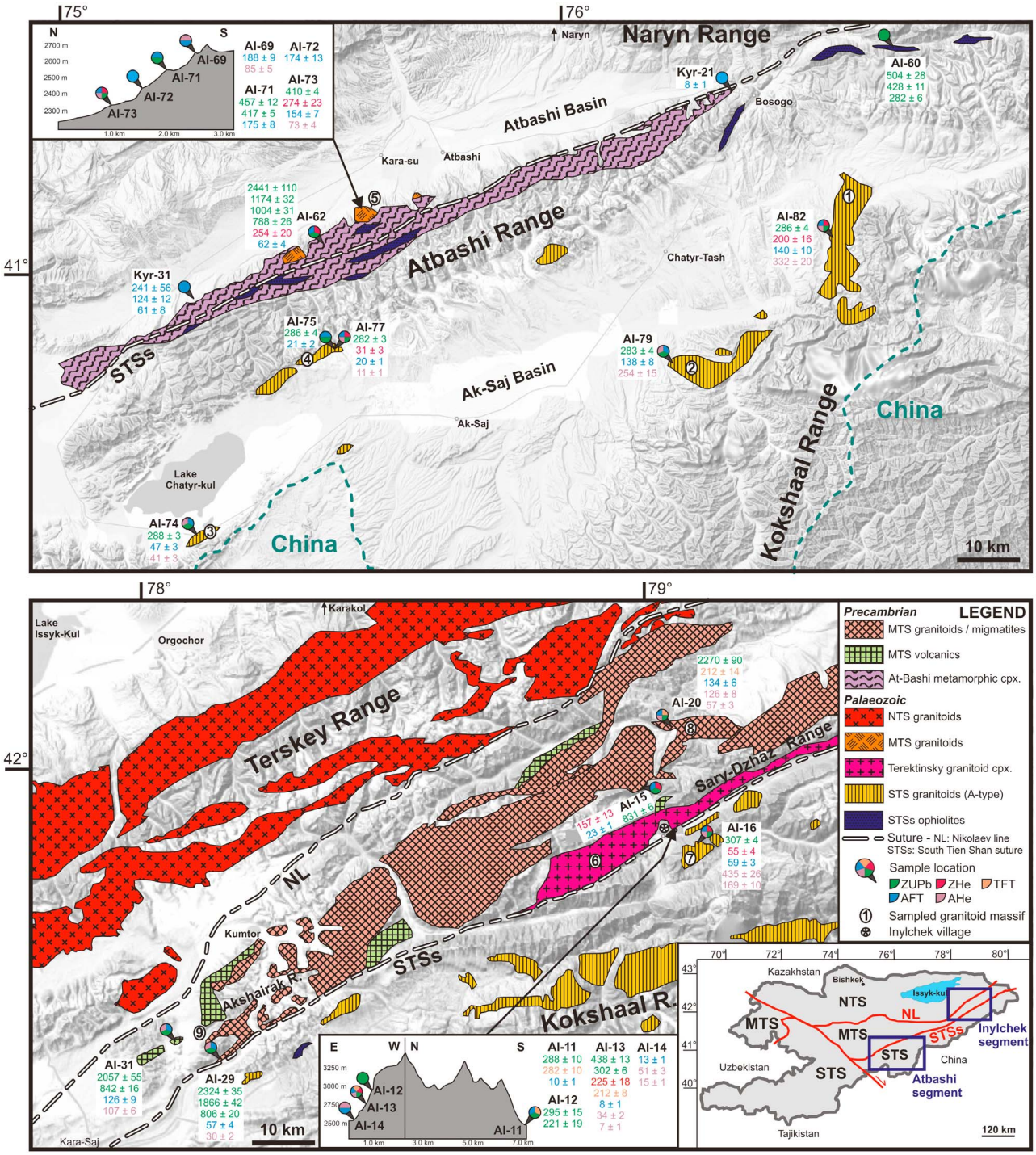

Figure 2. Digital terrain model of the (top) Atbashi and (bottom) Inylchek segments of the STSs showing their magmatic and metamorphic complexes. Points: 1 = Mudryum, 2 = Kok-Kiya, 3 = Torugart, 4 = Tashrabat, 5 = Kembel, 6 = Terektinsky, 7 = Tashkoro, 8 = Sary Dzhaz, 9 = Akshairak intrusive complexes [*Zhukov et al.*, 2008]. Sample sites and resulting ages (in Ma) are indicated and color-coded according to the applied dating method.

et al., 2004] was used as primary standard and Plešovice zircon [*Sláma et al.*, 2008] for validation purposes [*Glorie et al.*, 2011]. Data reduction was performed using the PepiAGE-software [*Dunkl et al.*, 2009] and the age results were plotted on a Wetherill concordia diagram using the Isoplot program [*Ludwig*, 2003].

3.2. Titanite Fission Track (TFT) Dating

[14] The titanite fission track method records the timing when the basement cooled below ~275–285°C [*Kohn et al.*, 1993; *Jacobs and Thomas*, 2001]. Resulting cooling ages generally correspond to post-magmatic or post-metamorphic

cooling of basement rocks in the lower crust. The latter process could for example mark the start of an exhumation event. Alternatively, the TFT system might be (partially) reset by an elevated geothermal gradient, e.g., induced by the transport of hot fluids through the basement. Three sample mounts were prepared for TFT dating following procedures described by *De Grave et al.* [2011a]. Spontaneous fission tracks were etched with a 0.4% HF solution for 24 h at 20°C, induced tracks in a muscovite detector with 40% HF for 40 min at 20°C. Irradiation was carried out in the Belgian Reactor 1 (BR1) facility of the Belgian Nuclear Research Centre in Mol (channel X26), where a thermal neutron fluence of 2.17×10^{15} cm^{-2} was achieved and monitored using metal activation monitors (diluted Co-Al and Au-Al foils). As for the AFT method (described below), counting was performed using an Olympus BH-2 microscope (1250 × magnification) equipped with transmitted and reflected light and drawing tube attachment. Both conventional ζ-ages (calibrated against IRMM 540 dosimeter glass) and Q-ages (based on the absolute neutron fluence) were calculated [*Wagner and Van den haute*, 1992]. A ζ-calibration value of 505.1 ± 7.8 $a.cm^2$ and a Q-factor of 1.910 ± 0.070 were obtained based on Fish Canyon Tuff and Mount Dromedary titanite age standards.

3.3. Zircon (U-Th)/He (ZHe) Dating

[15] The zircon (U-Th)/He dating method is complementary to the TFT method with respect to the closure-*T* and records cooling below ~170–190°C [*Reiners et al.*, 2004]. Recent studies on the KTB borehole (Germany) estimated more broadly that the ZHe system closes between ~200–130°C [*Wolfe and Stockli*, 2010]. Therefore, the ZHe method forms an important bridge between the high-*T* and low-*T* methods and can be considered as a connection between the titanite and apatite fission track methods. For seven samples, inclusion-free euhedral zircon grains (3 grains /sample) were wrapped separately in pre-cleaned (HCl; HNO_3) Pt-tubes. These triplicate aliquots for all seven samples were analyzed in the He-lab at the State University of Kansas (USA). The aliquots were degassed using a 20W Nd:YAG laser and ^{4}He was measured by isotope-dilution gas source mass-spectrometry, followed by U, Th and Sm concentration determination using isotope-dilution ICP-MS. Analytical details can be found in the work by *Wolfe and Stockli* [2010].

3.4. Apatite Fission Track (AFT) Thermochronometry

[16] The Apatite Fission Track method enables to reconstruct the thermal history of the host rocks between ~60–120°C [*Wagner and Van den haute*, 1992]. AFT cooling ages can be linked to movements in the upper-crust and correspond to exhumation and denudation of the sampled intrusions [e.g., *Sobel et al.*, 2006b; *De Grave et al.*, 2007; *Glorie et al.*, 2010]. A total of nineteen basement apatite samples and one additional sedimentary apatite sample were analyzed using the AFT-method. Spontaneous fission tracks in apatite were etched with a 2.5% (0.4M) HNO_3 solution for 70 s at 25°C, induced tracks in mica with 40% HF for 40 min at 20°C. Irradiation was also performed at BR1, using the same instrumental conditions as for the TFT samples. Both Q-ages (based on the calculated absolute thermal neutron fluence) and conventional ζ-ages (calibration factor based on IRMM 540 dosimeter glass) were calculated. A ζ-factor of 259.1 ± 3.3 $a.cm^2$ and a Q-factor of 1.001 ± 0.011 were obtained, based on Durango and Fish Canyon Tuff apatite age standards.

[17] AFT lengths were measured on horizontal confined fission tracks using an identical experimental setup as described by *Glorie et al.* [2010]. Where possible, 100 natural confined tracks were measured to construct an AFT length-frequency distribution, a number that was not always attained. Especially in the young samples, low track densities translate in insufficient numbers of measurable horizontal confined tracks. To enhance this number duplicate epoxy mounts were made for samples AI-13, 16, 20, 69, 73, 74, 77 and 82 (which hold the best quality apatites). These duplicates were wrapped in Al-foil (Al-degrader) and were irradiated with heavy ions at the linear accelerator of the Gesellschaft für Schwerionenforschung (GSI), Darmstadt, Germany [*Jonckheere et al.*, 2007], following identical analytical details as in the work by *De Grave et al.* [2011a]. Subsequent AFT thermal history modeling was carried out using the HeFTy software [*Ketcham*, 2005] with a fixed l_0 parameter of 15.95 μm [*Glorie et al.*, 2010]. The *tT* constraints were placed only where ZHe, AFT and/or AHe information was available. Additional D_{par} [*Donelick et al.*, 1999] measurements were carried out to monitor AFT annealing kinetics. The obtained D_{par} values were found to be identical to the values obtained for Durango apatite (~1.5 – 1.9 μm) [*Glorie et al.*, 2010; *De Grave et al.*, 2011a].

3.5. Apatite (U-Th)/He (AHe) Dating

[18] He-diffusion in apatite is blocked when the temperature drops below ~45–75°C. Therefore, the apatite (U-Th)/He (AHe) method is widely used in combination with the AFT method to refine the low-T thermal history [*Ehlers and Farley*, 2003]. Twelve apatite samples were prepared for AHe dating using the same preparation procedures as for the ZHe method. AHe analysis was also carried out in the He-lab of the State University of Kansas (USA) following analytical procedures as described by *Stockli et al.* [2000]. The resulting AHe ages were compared with AFT ages, obtained for the same samples. If the obtained AHe age exceeded its corresponding AFT age by more than 10%, the AHe age was regarded as being anomalous and therefore ignored. This anomalous behavior of the AHe dating method is a well-known phenomenon and might be explained by enhanced He retention in the apatite crystal lattice, especially, but not exclusively, for AHe ages > 100 Ma [*Green et al.*, 2006].

4. Results

[19] All results are plotted on the simplified geological map, showing the main igneous massifs along the Atbashi and Inylchek segments of the STSs (Figure 2).

4.1. Zircon U/Pb Ages

[20] The ZUPb results are summarized in Table 1, where arithmetic mean values are tabulated over all analyzed grains. A more detailed table, listing the results for each analyzed spot on every grain, can be found in Table S2 in the auxiliary material. Resulting concordia plots are presented in Figure 3. We subdivided the obtained ZUPb ages in three

Table 1. Zircon LA-ICP-MS U/Pb (ZUPb) Results[a]

Number	Sample	^{207}Pb[b] (cps)	U[c] (ppm)	Pb[c] (ppm)	Th/U[c]	$^{206}Pb/^{204}Pb$	$^{206}Pb/^{238}U$[d]	±2σ (%)	$^{207}Pb/^{235}U$[d]	±2σ (%)	$^{207}Pb/^{206}Pb$[d]	±2σ (%)	rho[e]	$^{207}Pb/^{238}Pb$[f]	±2σ (Ma)	$^{207}Pb/^{235}Pb$[f]	±2σ (Ma)	Con.[g]	N[h]	Con. Age[i] (Ma)	Note[j]	Loc.[k]
1	AI-20	8808	224	70	0.65	2739	0.2792	5.3	4.4268	7.7	0.1126	5.6	0.67	1584	72	1699	65	108	4	1087 ± 290	Lower-intercept	MTS
		22017	294	127	0.29	4829	0.3957	4.7	7.5439	5.9	0.1410	3.6	0.81	2149	87	2177	55	101	8	2270 ± 90	Upper-intercept	MTS
2	AI-31	5954	251	36	0.29	2971	0.1397	5.2	1.3180	7.3	0.0684	5.2	0.71	843	41	853	43	101	5	842 ± 16	Conc. component 1	MTS
		41644	300	125	0.27	5894	0.3717	6.2	6.5353	7.4	0.1383	4.0	0.82	2038	110	2050	68	101	4	2057 ± 55	Conc. component 2	MTS
3	AI-15	7813	416	58	0.35	7276	0.1380	3.8	1.2547	5.7	0.0659	4.0	0.68	833	30	825	32	99	19	831 ± 6	Concordant	MTS
4	AI-29	5162	351	48	0.42	2581	0.1321	3.7	1.2235	7.8	0.0674	6.1	0.46	800	28	811	45	101	4	806 ± 20	Conc. component 1	MTS
		19885	316	105	0.25	3758	0.3380	3.9	5.2178	12	0.1121	8.7	0.33	1877	64	1856	107	99	2	1866 ± 42	Conc. component 2	MTS
		16728	157	76	0.45	3284	0.4299	2.8	8.7956	15	0.1467	10	0.19	2305	55	2317	146	101	2	2324 ± 35	Conc. component 3	MTS
5	AI-62	6022	281	46	1.16	7246	0.1290	7.5	1.1863	10	0.0685	5.1	0.77	782	56	794	55	102	3	788 ± 26	Conc. component 1	MTS
		12425	465	86	0.66	6485	0.1693	5.5	1.6893	7.2	0.0724	4.6	0.76	1008	51	1004	47	100	5	1004 ± 31	Conc. component 2	MTS
		12359	347	72	0.49	7379	0.1973	6.0	2.1964	7.8	0.0807	4.9	0.77	1161	64	1179	56	102	7	1174 ± 32	Conc. component 3	MTS
		38750	310	127	0.53	5332	0.3578	5.4	7.1380	6.8	0.1385	4.2	0.80	1960	91	2080	62	107	6	2441 ± 110	Upper-intercept	MTS
7	AI-71	1089	358	27	0.58	1638	0.0670	4.3	0.5340	9.3	0.0578	8.2	0.47	418	17	434	34	104	19	417 ± 5	Conc. component 1	MTS
		327	137	11	0.58	341	0.0734	5.0	0.5443	20	0.0538	19	0.26	457	22	441	72	97	3	457 ± 12	Conc. component 2	MTS
8	AI-73	1090	198	15	0.64	2746	0.0657	5.1	0.5194	11	0.0573	9.6	0.48	410	20	425	39	103	22	410 ± 4	Concordant	MTS
9	AI-13	1956	435	23	0.53	3669	0.0480	5.5	0.3572	9.4	0.0540	7.3	0.62	302	16	310	25	103	12	302 ± 6	Conc. component 1	STSs
		2880	429	32	0.45	4296	0.0704	4.8	0.5526	6.7	0.0569	4.8	0.72	439	20	447	25	102	6	438 ± 13	Conc. component 2	STSs
10	AI-12	1991	351	18	0.51	1491	0.0458	8.7	0.3504	13	0.0557	10	0.63	289	24	305	36	106	6	295 ± 15	Conc. component 1	STSs
		4992	922	32	0.23	1557	0.0346	15	0.2477	18	0.0523	10	0.81	219	31	225	37	103	7	221 ± 19	Conc. component 2	STSs
11	AI-11	1719	458	21	0.29	2005	0.0458	7.8	0.3515	21	0.0566	18	0.47	289	22	305	55	106	8	288 ± 10	Conc. component 1	STSs
12	AI-60	1816	333	16	0.37	2939	0.0458	5.0	0.3446	11	0.0546	9.5	0.46	288	14	300	29	104	7	282 ± 6	Conc. component 1	STSs
		2652	299	22	0.49	6101	0.0688	4.6	0.5538	9.2	0.0584	7.9	0.51	429	19	447	34	104	6	428 ± 11	Conc. component 2	STSs
		2061	167	14	0.19	714	0.0813	4.3	0.7145	8.1	0.0638	6.9	0.54	504	21	547	35	109	3	504 ± 28	Conc. component 3	STSs
13	AI-16	1567	377	19	0.41	2621	0.0491	5.6	0.3567	10	0.0527	8.1	0.57	309	17	310	27	100	22	307 ± 4	Concordant	STS
14	AI-74	1147	397	19	0.46	2022	0.0457	4.2	0.3355	9.5	0.0532	8.4	0.47	288	12	294	24	102	21	288 ± 3	Concordant	STS
15	AI-75	2225	333	17	0.59	2268	0.0455	4.5	0.3408	8.2	0.0543	6.8	0.56	287	13	298	22	104	15	286 ± 4	Concordant	STS
16	AI-82	1977	429	20	0.44	2082	0.0453	4.9	0.3366	9.0	0.0539	7.2	0.52	285	14	295	23	103	14	286 ± 4	Concordant	STS
18	AI-79	1192	371	18	0.49	1681	0.0449	4.2	0.3295	10	0.0533	9.4	0.43	283	12	289	26	102	15	283 ± 4	Concordant	STS
19	AI-77	1307	332	16	0.40	2380	0.0448	4.5	0.3212	11	0.0520	10	0.45	283	13	283	27	100	22	282 ± 3	Concordant	STS

[a]For each parameter in the table, the arithmetic mean was calculated. A more detailed table is provided in the auxiliary material.
[b]Within-run, background-corrected mean ^{207}Pb signal.
[c]U and Pb content and Th/U ratio were calculated relative to the GJ-1 zircon standard.
[d]Corrected for: background, within-run Pb/U fractionation ($^{206}Pb/^{238}U$), where needed common Pb and subsequently normalized to GJ-1 (instrumental drift corrected).
[e]Rho is the error correlation defined as $err^{206}Pb/^{238}U/err^{207}Pb/^{235}U$.
[f]U/Pb ages were calculated with Isoplot [*Ludwig*, 2003].
[g]Degree of concordance = $age^{206}Pb/^{238}U/age^{207}Pb/^{206}Pb \times 100$.
[h]Number of targets (some grains yielded 2 targets).
[i]Concordant or Intercept age as calculated with Isoplot [*Ludwig*, 2003].
[j]Some samples yielded several components with respect to the concordia curve (intercept/concordant).
[k]Sample location in the Kyrgyz Tien Shan (NTS = North Tien Shan; MTS = Middle Tien Shan; STS = South Tien Shan; STSs = South Tien Shan suture).

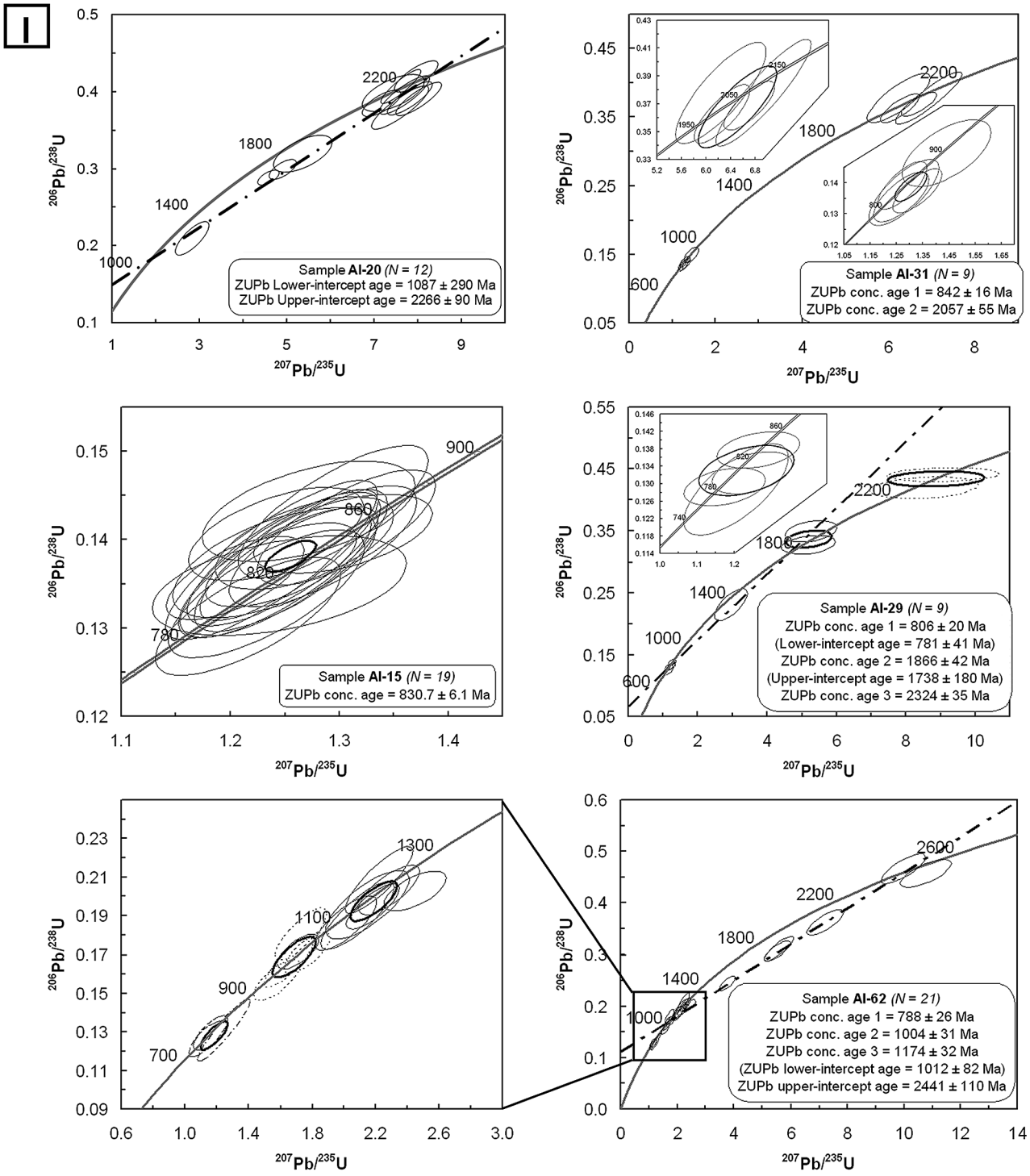

Figure 3. Shown are $^{206}Pb/^{238}U$ versus $^{207}Pb/^{235}U$ concordia plots [*Ludwig*, 2003], grouped according to the crystallization age of the analyzed samples (groups I, II, and III). All data-point error ellipses were calculated at the 2σ level. Where concordant ages were obtained, the central bold ellipses represent concordia ages with their 2σ uncertainty. Discordant ages are arranged along a discordia-line (bold dashed) and define upper- and lower-intercept ages with concordia.

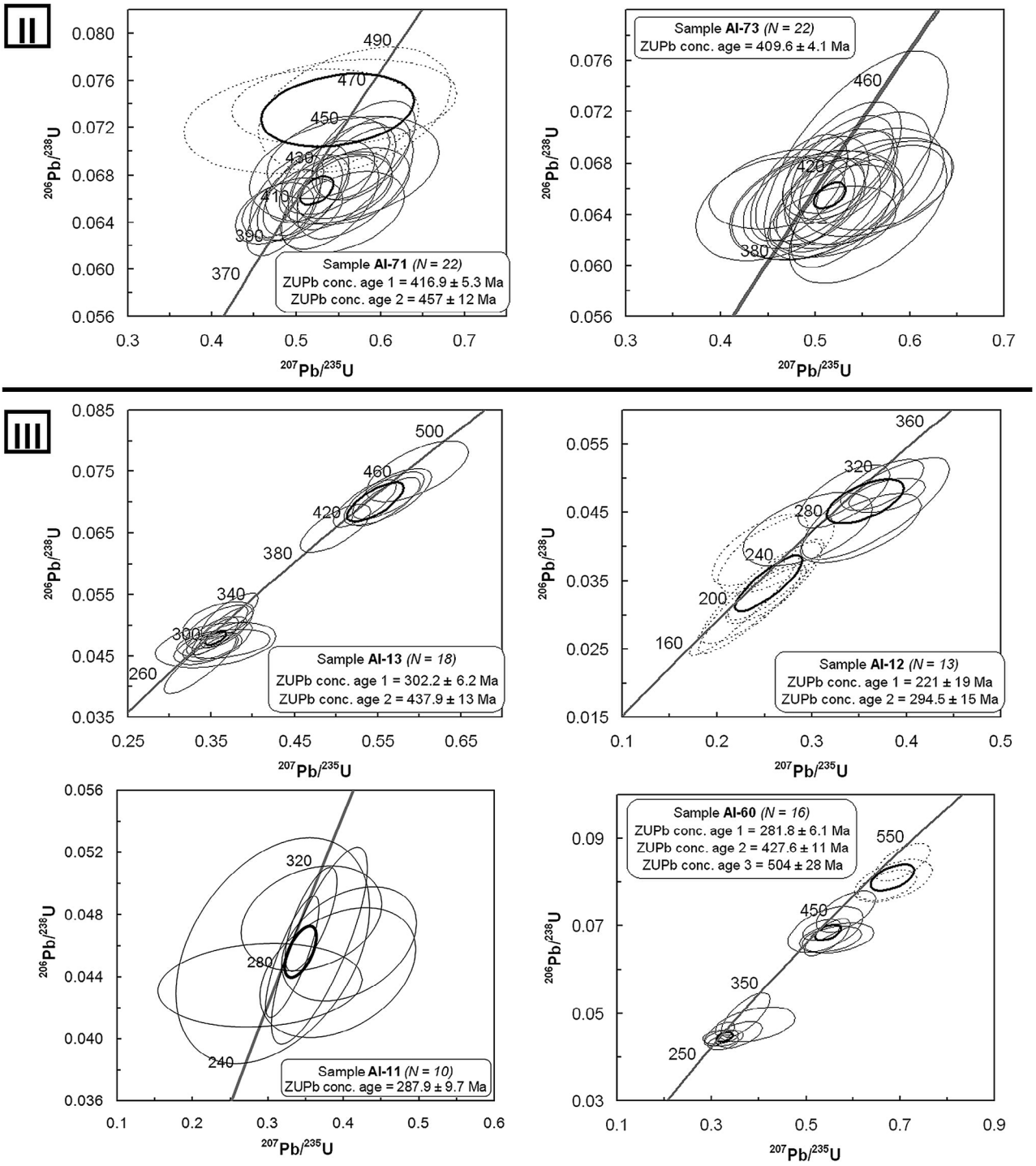

Figure 3. (continued)

groups according to their calculated crystallization age (i.e., their youngest concordant age component), corresponding to groups I–III in Figure 3. Within each group, the ages are also listed chronologically (Table 1 and Figure 3). As shown, in several samples multiple age components can be recognized, which are separately listed in Table 1. These older concordant age components are interpreted as recycled zircons that contain an inherited signal of more ancient zircon crystallization events.

4.1.1. Precambrian ZUPb Ages

[21] Group 'I' contains the ZUPb results obtained for four Precambrian granitoids (AI-15, 20, 29, 31) and one gneiss (AI-62). These were sampled north of the STSs, in the MTS terrane. The zircons of sample AI-20 define a discordia-line

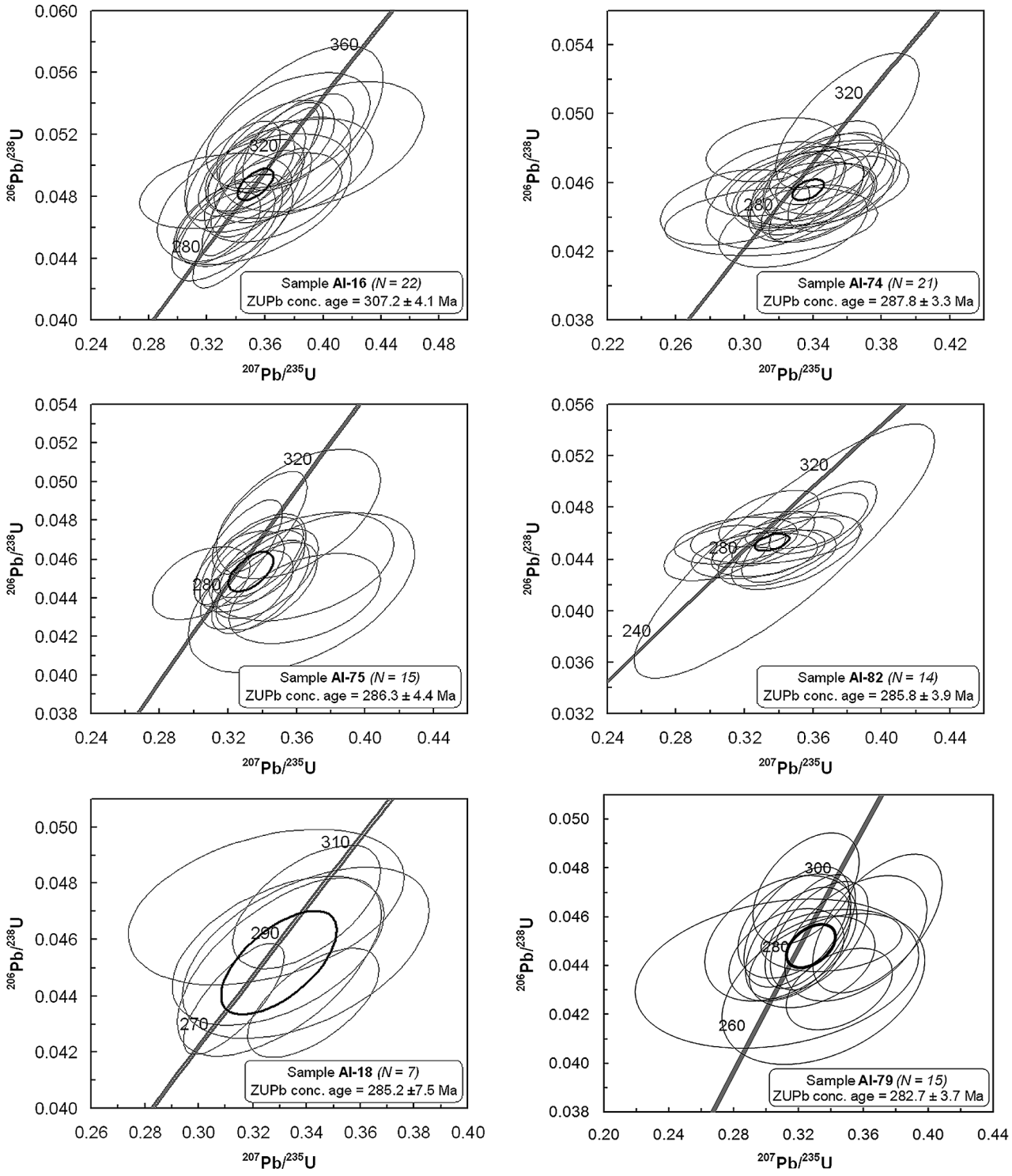

Figure 3. (continued)

with a main group of data points clustering around an upper-intercept age of 2270 ± 90 Ma. No concordant age can be obtained for this data cluster. Only 4 zircons differ from the main age cluster, which results in a large uncertainty on the lower-intercept age (1087 ± 290 Ma). Sample AI-31 yields two distinct sets of concordant ages of respectively 2057 ± 55 Ma and 842 ± 16 Ma. The Neo-Proterozoic age component is equal within error to the concordant age of sample AI-15 (831 ± 6 Ma) and the youngest concordant age components of sample AI-29 (806 ± 20 Ma). Sample AI-29 further contains a few Paleo-Proterozoic zircons with concordant age components of 1866 ± 42 Ma and 2324 ± 35 Ma. Gneiss-sample AI-62 from the Atbashi metamorphic complex yields one concordant Neo-Proterozoic

Table 2a. Results for Apatite (AFT) Fission Track Analyses

Sample	n[a]	ρ_s ($\pm1\sigma$)[b]	N_s[c]	ρ_i ($\pm1\sigma$)[b]	N_i[c]	ρ_d ($\pm1\sigma$)[b]	N_d[c]	ρ_s/ρ_i	P(χ^2)[d]	t(ζ)[e]	t(Q)[e]	l_m[f]	n_l[f]	σ[f]
AI-20*	30	13.979 (0.270)	2684	5.823 (0.174)	1118	4.247 (0.105)	1631	2.451 ± 0.087	1.00	133.5 ± 6.0	133.0 ± 6.0	13.2	58	1.4
AI-15	70	1.544 (0.061)	642	3.578 (0.093)	1491	4.018 (0.112)	1285	0.442 ± 0.021	1.00	23.0 ± 1.3	23.3 ± 1.3	-	-	-
AI-14	48	1.228 (0.066)	345	5.651 (0.143)	1560	4.252 (0.105)	1633	0.233 ± 0.014	0.99	12.8 ± 0.8	12.8 ± 0.8	-	-	-
AI-13*	75	0.711 (0.040)	309	5.061 (0.108)	2187	4.255 (0.105)	1634	0.143 ± 0.009	1.00	7.9 ± 0.5	7.8 ± 0.5	12.6	46	1.3
AI-11	20	1.184 (0.118)	101	6.662 (0.283)	555	4.006 (0.112)	1282	0.188 ± 0.020	0.98	9.8 ± 1.1	9.9 ± 1.1	-	-	-
AI-16*	55	4.984 (0.123)	1655	4.637 (0.118)	1533	4.250 (0.105)	1632	1.074 ± 0.038	1.00	58.9 ± 2.7	58.7 ± 2.6	13.5	31	1.2
AI-31	35	5.309 (0.184)	832	2.308 (0.122)	356	4.240 (0.105)	1629	2.317 ± 0.147	1.00	126.1 ± 8.7	128.5 ± 8.9	13.0	32	1.0
AI-29	35	3.628 (0.159)	519	3.615 (0.161)	504	4.230 (0.105)	1627	1.034 ± 0.065	1.00	56.5 ± 3.9	57.7 ± 3.9	-	-	-
AI-73*	30	28.308 (0.490)	3389	10.026 (0.290)	1195	4.227 (0.105)	1623	2.843 ± 0.096	0.97	153.9 ± 6.7	152.5 ± 6.6	14.1	100	1.0
AI-72	18	30.283 (1.015)	890	9.419 (0.562)	281	4.231 (0.105)	1625	3.213 ± 0.220	0.91	173.8 ± 13	172.3 ± 13	-	-	-
AI-71	25	33.586 (0.575)	3408	10.495 (0.322)	1065	4.234 (0.105)	1626	3.236 ± 0.114	0.95	175.1 ± 7.9	173.8 ± 7.7	14.1	32	0.7
AI-69	35	24.631 (0.451)	2985	7.192 (0.244)	869	4.237 (0.105)	1627	3.471 ± 0.134	1.00	187.8 ± 8.9	186.5 ± 8.8	14.0	78	0.8
AI-62	45	2.271 (0.098)	532	1.889 (0.090)	444	4.042 (0.112)	1293	1.191 ± 0.077	1.00	62.1 ± 4.4	62.5 ± 4.4	-	-	-
Kyr-21	20	1.330 (0.128)	108	8.883 (0.333)	711	4.192 (0.104)	1611	0.154 ± 0.016	0.89	8.4 ± 0.9	8.6 ± 0.9	-	-	-
AI-75	35	1.334 (0.098)	187	3.590 (0.159)	508	4.212 (0.105)	1617	0.385 ± 0.033	1.00	21.0 ± 1.9	20.7 ± 1.9	-	-	-
AI-77*	55	2.634 (0.113)	540	7.571 (0.190)	1592	4.209 (0.105)	1616	0.358 ± 0.018	1.00	19.5 ± 1.1	19.2 ± 1.1	13.0	100	1.6
AI-74*	40	4.122 (0.136)	924	4.777 (0.147)	1061	4.223 (0.105)	1622	0.869 ± 0.039	1.00	47.4 ± 2.5	46.9 ± 2.5	12.7	93	1.4
AI-79	50	5.082 (0.135)	1422	2.002 (0.085)	557	4.207 (0.105)	1615	2.564 ± 0.128	1.00	138.2 ± 7.9	136.2 ± 7.8	13.1	41	1.0
AI-82*	30	9.293 (0.330)	795	3.632 (0.207)	309	4.205 (0.105)	1615	2.588 ± 0.174	0.99	139.5 ± 10	137.4 ± 10	12.9	100	1.6
Kyr-31	6	5.825 (0.574)	103	1.297 (0.271)	23	4.202 (0.105)	1614	4.502 ± 1.038	1.00	240.6 ± 56	247.3 ± 57	-	-	-
	25	4.463 (0.217)	422	1.968 (0.147)	179	4.202 (0.105)	1614	2.302 ± 0.205	0.99	124.1 ± 12	127.7 ± 12			
	18	2.513 (0.207)	147	2.303 (0.200)	132	4.202 (0.105)	1614	1.120 ± 0.134	1.00	60.7 ± 7.5	62.4 ± 7.7			

[a]The variable n is the number of analyzed grains.
[b]The values ρ_s, ρ_i, and ρ_d are the density of spontaneous, induced tracks and induced tracks in an external detector (ED) irradiated against a dosimeter glass (IRMM-540). For the AFT results, all track densities are expressed as 10^5 tracks/cm^2.
[c]N_s, N_i, and N_d are the number of counted spontaneous, induced tracks and induced tracks in the ED.
[d]P(χ^2) is the chi-squared probability that the dated grains have a constant ρ_s/ρ_i-ratio.
[e]The values t(ζ) and t(Q) give the resulting ages, expressed in Ma.
[f]AFT length data are reported as a mean track length (l_m) with standard deviation σ, obtained from the measurement of a number (n_l) of natural, horizontal confined tracks. For samples indicated by an asterisk, heavy ion irradiation was used to enhance the number of measurable horizontal confined tracks. See text for more details.

(788 ± 26 Ma) and two Meso-Proterozoic (1004 ± 31 Ma; 1174 ± 32 Ma) components. Older zircons for this sample align along a discordia line with an upper-intercept age of 2441 ± 110 Ma. In summary, the MTS complexes for group I yield three distinct zircon populations with Rodinia break-up (~850–770 Ma) crystallization ages and Grenvillian (~1200–1000 Ma) and Palaeo-Proterozoic (~2500–1850 Ma) inherited ages.

4.1.2. Caledonian ZUPb Ages

[22] Group 'II' consists of two granitoid samples (AI-71, 73) from the Kembel massif, just north of the Atbashi metamorphic complex (Figure 2). Sample AI-73 yields a concordant ZUPb age of 410 ± 4 Ma, which is within error of the youngest age component of AI-71 (417 ± 5 Ma). In the latter sample some older grains were found as well (common-Pb corrected concordant age: 457 ± 12 Ma). These however suffer from relatively higher common-Pb concentrations (low $^{206}Pb/^{204}Pb$ ratio in Table 1). Therefore, caution is needed when interpreting this apparent concordant age, as it might slightly overestimate the true age for this zircon population. These results point toward a distinct granitoid intrusion episode during the Late Caledonian (~420–405 Ma), just North of the Kyrgyz STSs. This is a surprising and important new observation. Hitherto it was always assumed that Caledonian magmatism was strictly limited to the NTS. Here, we hence provide evidence that, albeit more restricted, Caledonian plutons do occur in the MTS.

4.1.3. Hercynian ZUPb Ages

[23] Group 'III' is composed of granitoid samples which were taken within or just south of the STSs. More specifically, this group consists of (1) three samples (AI-11, 12, 13) from the Terektinsky granitoid complex at the northern edge of the Inylchek segment; (2) tonalite sample (AI-60) which intruded the Atbashi ophiolites and (3) granitoid samples from the A-type STS intrusions (AI-16, 74, 75, 77, 79, 82) (Figure 2). Within error, samples AI-11, 12 and 13 yield a

Table 2b. Results for Titanite (TFT) Fission Track Analyses

Sample	n[a]	ρ_s ($\pm1\sigma$)[b]	N_s[c]	ρ_i ($\pm1\sigma$)[b]	N_i[c]	ρ_d ($\pm1\sigma$)[b]	N_d[c]	ρ_s/ρ_i	P(χ^2)[d]	t(ζ)[e]	t(Q)[e]
AI-20	12	2.649 (0.094)	794	1.267 (0.064)	392	4.016 (0.079)	2569	2.120 ± 0.131	0.27	211.5 ± 14	210.2 ± 16
AI-13	20	15.759 (0.228)	4802	7.435 (0.154)	2329	4.006 (0.079)	2558	2.128 ± 0.054	0.12	211.8 ± 7.5	210.9 ± 11
AI-11	20	15.980 (0.224)	5115	5.834 (0.135)	1867	4.010 (0.079)	2567	2.856 ± 0.077	0.07	282.3 ± 10	281.5 ± 15

[a]The variable n is the number of analyzed grains.
[b]The values ρ_s, ρ_i, and ρ_d are the density of spontaneous, induced tracks and induced tracks in an external detector (ED) irradiated against a dosimeter glass (IRMM-540). For the TFT results, ρ_s and ρ_i are expressed as 10^6 tracks/cm^2, ρ_d as 10^5 tracks/cm^2.
[c]N_s, N_i, and N_d are the number of counted spontaneous, induced tracks and induced tracks in the ED.
[d]P(χ^2) is the chi-squared probability that the dated grains have a constant ρ_s/ρ_i-ratio.
[e]The values t(ζ) and t(Q) give the resulting ages, expressed in Ma.

Table 3a. Results for Apatite (AHe) (U-Th)/He Analyses

Sample	U[a]	Th[a]	Sm[a]	Th/U	He[b]	m[c]	F_T[d]	Age[e]	Average[e]	AFT Age[f]
AI-20	1.6	0.8	3.5	0.5	0.41	5.0	0.76	57.0 ± 3.4	57.0 ± 3.4	
	1.9	2.6	46.9	1.4	1.25	3.1	0.69	117.6 ± 7.1		
	21.1	7.5	16.3	0.4	12.14	4.3	0.73	133.7 ± 8.0	125.7 ± 7.5	133.5 ± 6.0
AI-14	13.1	19.6	102.6	1.5	1.12	7.1	0.75	14.8 ± 0.9		
	8.5	25.1	112.8	3.0	0.92	6.4	0.75	14.9 ± 0.9	14.9 ± 0.9	12.8 ± 0.8
	14.6	26.5	120.4	1.8	4.46	5.7	0.74	50.6 ± 3.0	50.6 ± 3.0	
AI-13	8.3	31.5	92.2	3.8	0.43	5.8	0.74	6.6 ± 0.4	6.6 ± 0.4	
	11.1	37.0	135.0	3.3	2.55	3.6	0.69	32.4 ± 1.9		
	9.7	28.5	91.4	2.9	2.50	8.3	0.77	35.2 ± 2.1	33.8 ± 2.0	7.9 ± 0.5
AI-16	50.1	602.8	187.9	12.0	133.9	7.4	0.75	169.0 ± 10	169.0 ± 10	
	34.5	97.3	225.1	2.8	113.5	12.7	0.80	434.5 ± 26		
	17.3	66.8	229.4	3.9	58.99	3.9	0.70	435.5 ± 26	435.0 ± 26	58.9 ± 2.7
AI-31	7.6	9.7	20.4	1.3	4.29	8.9	0.78	101.8 ± 6.1		
	2.2	5.9	12.9	2.6	1.54	5.1	0.74	102.9 ± 6.2		
	8.8	14.8	21.5	1.7	6.21	9.5	0.78	116.7 ± 7.0	107.1 ± 6.4	126.1 ± 8.7
AI-29	9.3	28.6	25.1	3.1	1.50	2.6	0.67	25.3 ± 1.5		
	7.1	22.9	22.5	3.2	1.18	3.0	0.68	25.4 ± 1.5		
	4.5	19.4	13.4	4.3	1.46	5.6	0.74	39.3 ± 2.4	30.0 ± 1.8	56.5 ± 3.9
AI-73	2.5	3.7	4.7	1.5	0.93	9.0	0.78	64.7 ± 3.9		
	0.5	1.5	2.6	2.8	0.29	25.5	0.83	68.9 ± 4.1		
	1.4	2.4	3.6	1.7	0.76	17.7	0.82	86.0 ± 5.2	73.2 ± 4.4	153.9 ± 6.7
AI-69	0.5	0.2	2.0	0.3	0.01	*1.8*	0.65	5.3 ± 0.3	Reject	
	23.5	48.6	86.3	2.1	9.81	1.4	0.61	83.2 ± 5.0		
	24.6	39.5	79.2	1.6	8.54	0.6	0.51	86.9 ± 5.8	85.1 ± 5.4	187.8 ± 8.9
AI-77	26.2	29.8	74.7	1.1	1.34	4.3	0.72	10.2 ± 0.6		
	31.0	38.6	95.2	1.2	1.68	4.7	0.72	10.6 ± 0.6		
	25.8	34.9	101.6	1.4	1.59	5.4	0.74	11.4 ± 0.7	10.7 ± 0.6	19.5 ± 1.1
AI-74	16.6	57.5	254.4	3.5	4.49	8.9	0.78	33.1 ± 2.0		
	13.9	46.7	185.6	3.4	5.08	16.8	0.82	43.5 ± 2.6		
	24.3	86.6	298.1	3.6	9.53	12.6	0.78	47.8 ± 2.9	41.4 ± 2.5	47.4 ± 2.5
AI-79	1.6	6.3	82.3	4.0	3.54	5.3	0.74	235.3 ± 14		
	2.2	9.3	93.4	4.2	5.74	8.5	0.77	263.1 ± 15		
	3.4	12.5	104.0	3.7	7.75	6.1	0.75	263.8 ± 15	254.1 ± 15	138.2 ± 7.9
AI-82	3.2	18.4	28.1	5.8	10.30	10.4	0.78	312.8 ± 18		
	0.7	2.9	12.9	4.4	1.93	3.2	0.68	351.1 ± 21	331.9 ± 19	

[a]Concentrations for U, Th and Sm are listed in ppm.
[b]The ^{4}He concentration is in ncc/μg.
[c]The mass (m) of the apatite grains is in μg.
[d]F_T is the ejection correction factor.
[e]For each sample, three single grain ages (triplicate aliquots) were obtained and where consistent data was found, an average value was calculated (in Ma).
[f]AFT ages are listed as well for comparison with the AHe data. AHe ages were not discussed further if they exceeded their corresponding AFT age by more than 10% (see text).

similar major concordant age component of ~310–285 Ma. In addition, AI-12 exhibits a younger age-component of ~220 Ma. The occurrence of these younger, Triassic zircons would question whether the crystallization age of the Terektinsky complex should indeed be assigned to the Late Carboniferous–Early Permian as is generally accepted. The Triassic zircons of AI-12 however exhibit a lower average Th/U ratio (0.23) in comparison to the Late Paleozoic zircons from this sample (0.51) (Table 1). Since no signs of metamorphism were observed in outcrop, nor found in the thin-section and CL-images for this sample, we consider the deviant Th/U ratio to be an effect of hydrothermal zircon growth [*Hoskin and Schaltegger*, 2003]. The ablation spots for the Triassic ZUPb ages are indeed located mainly on the rims of the crystals, where the effect of hydrothermal activity is most pronounced. More evidence in support of this hypothesis comes from the TFT data for the Terektinsky profile (discussed below).

[24] Clearly differing from its main Hercynian concordant crystallization age, Sample AI-13 yields a secondary Caledonian age component (438 ± 13 Ma). Tonalite sample AI-62 even yields three distinct concordant age components of 282 ± 6 Ma, 428 ± 11 Ma and 504 ± 28 Ma. All analyzed grains of this sample show magmatic oscillatory zonation and are characterized by typical magmatic Th/U ratios between 0.25 and 0.5 (Table 1). The youngest zircons date the intrusion of the tonalite in the ophiolite, while the older zircons are recycled. Samples AI-74, 75, 77, 79, 82 from the A-type granitoid intrusions in the STS tectonic unit (south of the suture) [*Konopelko et al.*, 2007, 2009] yield a single concordant crystallization age in a narrow time-span of ~290–280 Ma. For sample AI-16 from the Tashkoro intrusion we obtained a concordant crystallization age of 307 ± 4 Ma (Figure 2).

[25] In summary, Late Carboniferous–Early Permian crystallization ages were obtained for post-collisional granitoids within or south of the STSs. Some samples show Caledonian inherited components, while others yield Triassic zircon rims presumably due to hydrothermal activity.

4.2. Titanite Fission Track and Zircon (U-Th)/He Results

[26] TFT and ZHe ages are presented for one profile across the Atbashi and one across the Inylchek segment of

Table 3b. Results for Zircon (ZHe) (U-Th)/He Analyses

Sample	U[a]	Th[a]	Sm[a]	Th/U	He[b]	m[c]	F_T[d]	Age[e]	Average[e]
AI-15	515.5	167.7	3.1	0.33	350.6	9.71	0.79	146.5 ± 12	
	519.0	212.6	1.9	0.41	398.6	12.95	0.80	161.3 ± 13	
	369.6	124.8	0.8	0.34	308.4	44.23	0.88	161.7 ± 13	156.5 ± 12
AI-13	491.9	287.4	3.1	0.58	500.7	8.35	0.79	208.1 ± 17	
	380.7	216.2	2.0	0.57	423.4	10.54	0.80	224.7 ± 18	
	234.4	161.3	1.5	0.69	286.4	11.48	0.79	243.4 ± 20	225.4 ± 18
AI-16	1959	738.5	5.6	0.38	496.1	31.55	0.85	50.6 ± 4.1	
	1739	572.7	7.0	0.33	465.1	34.38	0.86	53.4 ± 4.3	
	1989	846.2	13.0	0.43	621.3	28.03	0.84	62.2 ± 5.0	55.4 ± 4.4
AI-73	162.7	92.1	1.5	0.57	181.5	4.86	0.73	259.8 ± 21	
	140.1	88.6	0.5	0.63	152.5	2.41	0.67	264.2 ± 26	
	187.7	169.9	1.8	0.91	235.4	2.28	0.63	298.0 ± 24	274.0 ± 23
AI-62	404.2	200.4	6.1	0.50	397.8	1.66	0.65	249.7 ± 20	
	435.1	205.4	15.6	0.47	486.1	2.68	0.71	257.5 ± 21	253.6 ± 20
AI-77	739.6	267.4	1.0	0.36	108.8	40.25	0.87	28.7 ± 2.3	
	132.7	59.9	0.8	0.45	21.2	33.08	0.87	30.9 ± 2.5	
	692.2	278.1	1.3	0.40	117.8	19.98	0.85	34.0 ± 2.7	31.2 ± 2.5
AI-82	718.4	273.8	3.8	0.38	536.7	2.19	0.69	181.2 ± 15	
	455.4	218.1	4.6	0.48	361.8	1.83	0.68	192.9 ± 15	
	546.8	289.6	5.4	0.53	550.3	3.08	0.72	225.9 ± 18	200.0 ± 16

[a]Concentrations for U, Th and Sm are listed in ppm.
[b]The ^{4}He concentration is in ncc/μg.
[c]The mass (m) of the apatite grains is in μg.
[d]F_T is the ejection correction factor.
[e]For each sample, three single grain ages (triplicate aliquots) were obtained and where consistent data was found, an average value was calculated (in Ma).

the STSs (Figure 2 and Tables 2a, 2b, 3a, and 3b). North of the STSs, all ages except one cluster between the Permian and Triassic (~290–200 Ma). Sample AI-15 is the outlier with a Late Jurassic ZHe age of ~160 Ma (Figure 2 and Table 3b). The TFT age of sample AI-11 is the oldest (~290 Ma) in this interval, and this age is within uncertainty the same as its concordant ZUPb age. This observation indicates that the Terektinsky complex cooled very fast from zircon crystallization temperatures (>800°C) to TFT closure temperatures (~265–310°C) and was thus likely emplaced at high crustal levels. It further underscores that the Terektinsky complex granitoids were already emplaced in the Early Permian. Sample AI-13 yields within error identical Triassic ZHe and TFT ages which furthermore correspond to the youngest (Triassic) concordant ZUPb age component of sample AI-12. This supports the hypothesis that the Terektinsky complex was subjected to hydrothermal fluids in the Triassic. Hot fluid circulation in the Terektinsky complex seems to have affected the zircons of sample AI-12 and reset the TFT and ZHe chronometers during the Middle–Late Triassic (~230–210 Ma). Sample AI-20 yields an identical TFT age as sample AI-13, which might suggest that a similar Triassic (hydrothermal) heat source has also reset the TFT system more to the north of the STSs. The ZHe ages of the Atbashi metamorphic complex and the neighboring Ashukultor subvolcanic complex (~280–250 Ma) are identical within error and probably record the first signs of Late Paleozoic exhumation (Figure 2). The Late Jurassic (~160 Ma) ZHe age of sample AI-15 is probably a mixed age between the Late Paleozoic and Mesozoic exhumation events (discussed below).

[27] South of the STSs, samples AI-16 and AI-77 yield Early (~55 Ma) and Late (~30 Ma) Paleogene ZHe ages respectively (Figure 2 and Table 3b). These ages provide evidence for Cenozoic reactivation, focused within the STSs. This observation will be explored more extensively in combination with the AFT data set (discussed below). Further south, sample AI-82 was dated at ~200 Ma (TFT) and shows a closer affinity with TFT ages north of the STSs.

4.3. Apatite Fission Track and Apatite (U-Th)/He Results

[28] Nineteen AFT ages and twelve AHe ages were obtained for basement samples along traverses and vertical profiles across the Kyrgyz STSs. Analytical details can be found in Tables 2a and 3a, where the samples are geographically divided into the Atbashi and Inylchek segments. For each segment, the samples are arranged from north to south across the Kyrgyz STSs. Q- and ζ- AFT ages are all identical within uncertainty. The conventional ζ-ages will be used in further discussion. The obtained AFT and AHe ages range between the Jurassic and the Late Miocene (~190–6 Ma).

[29] Four samples from the Kembel massif (Atbashi segment) record the oldest ~190–150 Ma (Jurassic) AFT ages of the study area. The individual AFT ages reveal a normal age-elevation relationship for the ~300 m sampling elevation difference with the youngest sample (AI-73; ~154 Ma) at the bottom and the oldest sample (AI-69; ~188 Ma) at the top (Figure 2). For two samples from this massif, Late Cretaceous (~85–70 Ma) AHe ages were obtained which are thus significantly younger than the corresponding AFT ages. Confined track length measurements yield mean lengths of 14.0–14.1 μm and narrow (σ = 0.7–1.0 μm), symmetrical length frequency distributions (Table 2a and Figure 4).

[30] Just south of the Kembel massif, in the Atbashi metamorphic complex, an Early Paleogene AFT age was obtained (AI-62; ~62 Ma). Further southeast in the STSs itself, sample Kyr-21 yielded a Late Miocene AFT-age of ~8 Ma. Due to the limited amount of good quality apatites, no length measurements, nor AHe ages could be obtained for these samples.

[31] South of the Atbashi STSs segment, two samples from the Tashrabat intrusive (AI-75, 77) were analyzed by

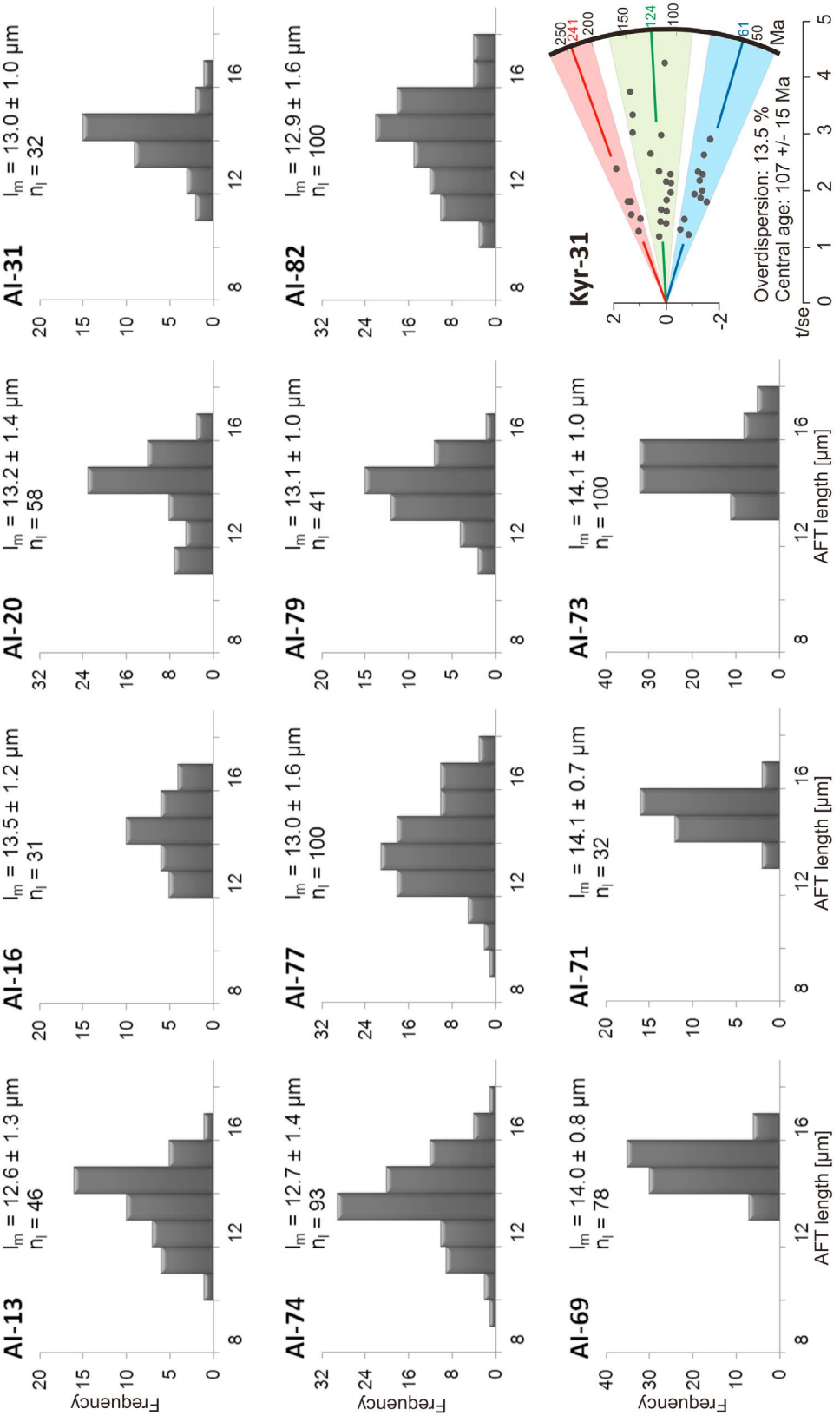

Figure 4. Apatite fission track (AFT) length frequency distributions. l_m represents the mean AFT length with its 1σ standard deviation. n_l = number of measured horizontal confined tracks. The radial plot for sample Kyr-31 in the lower right corner indicates three detrital components based on apatite color and morphology. See text for more details.

the AFT and AHe methods (Figure 2 and Tables 2a and 3a). Early Miocene (~19–21) AFT ages and a Late Miocene (~11 Ma) AHe age were obtained. The AFT length frequency distribution is broad in comparison with those obtained for the Kembel massif (Figure 4). The mean length of 13.0 ± 1.6 μm also clearly differs from the Kembel AFT length observations. Further south, in the Kokshaal Range at the Kyrgyz-Chinese border, sample AI-74 (Torugart massif) yields Eocene AFT (~47 Ma) and AHe (~41 Ma) ages (Figure 2 and Tables 2a and 3a). Samples AI-79 (Kok-Kiya intrusion) and AI-82 (Mudryum intrusion) to the east of the latter sample, yield consistent AFT ages of ~140 and ~138 Ma. Their corresponding AHe ages gave anomalously old results of ~254 Ma and ~332 Ma respectively and are therefore not discussed further. AFT length measurements for the Torugart, Kok-Kiya and Mudryum samples are similar to those obtained for the Tashrabat sample, with mean values of 12.9–13.1 μm and σ varying between 1.0 and 1.6 μm (Table 2a and Figure 4).

[32] In the Inylchek segment, two samples (AI-29, 31) from the western foothills of the Akshairak Range were prepared for AFT and AHe dating. AI-29 was sampled at the northern edge of the STSs and yielded an Early Paleogene (~57 Ma) AFT age, similar as for sample AI-62 in the Atbashi metamorphic complex. Its AHe age was calculated at ~30 Ma (Oligocene). Sample AI-31 is situated about 6 km north of the suture and yields an AFT age of ~126 Ma, which corresponds to the Early Cretaceous AFT ages of samples AI-79 and AI-82, south of the Atbashi STSs segment. The AFT length data (13.0 ± 1.0 μm) is also very similar to that of samples AI-79 and 82. The AHe age of sample AI-31 was found to be ~107 Ma, i.e., slightly younger than its corresponding AFT age (Figure 2 and Tables 2a and 3a).

[33] Further east along the Inylchek segment of the STSs, a N-S transect was sampled, including a vertical profile in the Terektinsky granitoid complex (Figure 2). The northernmost sample AI-20 yielded an Early Cretaceous AFT age (~135 Ma). This corresponds to other samples (AI-31, 79, 82) in the vicinity (both north and south) of the STSs (Figure 2 and Table 2a). For AI-20, a relative broad length distribution was obtained with a mean length of 13.2 ± 1.4 μm. The AHe results for this sample show two consistent Cretaceous ages (~135–115 Ma) and one younger, Early Paleogene age (~57 Ma) (Table 3a). The Cretaceous AHe age (based on two aliquots) and the obtained AFT age are identical within error. The youngest AHe age (1 grain) corresponds to AFT and AHe ages obtained closer to the STSs (samples AI-62, 29). For sample AI-15 an Early Miocene AFT age (~23 Ma) was obtained which corresponds to the AFT age of samples AI-75 (~21 Ma) and AI-77 (~20 Ma). South of the STSs, an Early Paleogene AFT age (~59 Ma) was found as well (sample AI-16; Tashkoro intrusion). The AFT age for the latter sample lies close to its ZHe age, indicating rapid cooling of the Tashkoro intrusion during this time-interval. Although only a limited amount of confined fission tracks could be measured, AFT lengths for sample AI-16 are relatively long (13.5 ± 1.2 μm) and therefore confirm this observation. No meaningful AHe age could be obtained for this sample (Table 3a).

[34] For the Terektinsky profile, three AFT-ages were obtained and range between ~13–8 Ma. Sample AI-13 exhibits an asymmetric length distribution with a relatively low mean value (12.6 ± 1.3 μm), testifying to a more complex Cenozoic thermal history. This observation is further supported by the occurrence of two AHe components in samples AI-13 and AI-14. For sample AI-13, two AHe analyses yield an older (~34 Ma) age, while one aliquot gives ~7 Ma, which is identical to its AFT age. For sample AI-14, two grains yielded a consistent AHe result of ~15 Ma, which is in good agreement with the AFT age. One grain however gave an anomalously older AHe age of ~51 Ma. These older AHe age components might indicate a preserved Paleogene cooling signal for the Terektinsky complex.

[35] As mentioned previously, one additional detrital (conglomerate) sample (Kyr-31) was collected. This sample comes from the Paleogene *Kokturpak Formation* [*Cobbold et al.*, 1994; *Zhukov et al.*, 2008], just north of the Atbashi metamorphic complex (Figure 2 and Tables 2a and 2b). The AFT data for this sample exhibits a relative large degree of overdispersion (~14%) (Figure 4). This might point to the existence of more than one AFT age component. Radialplotter [*Vermeesch*, 2009] could not distinguish statistical different age populations and returned only a single AFT age of 107 ± 8 Ma. When reviewing the data however, one can recognize three possible trends in the data set, with two well-pronounced AFT age groups of ~61 Ma (n = 18) and ~124 Ma (n = 25), and a possible third age component of ~241 Ma that groups six older grains with consistent ρ_s/ρ_i ratios. Differences in grain morphology between apatites defining these supposed age groups are present, albeit quite subtle. The youngest apatite crystals (~61 Ma trend) are more idiomorphic than the older grains (which are more subrounded). The apatites from the oldest group (~241 Ma trend) consistently show a more yellowish color in comparison to the colorless younger grains. We therefore further discuss the detrital AFT ages as distinct components, indicating different source areas with varying cooling histories.

5. Interpretation and Discussion

5.1. Tien Shan Amalgamation and STSs Formation: Zircon U/Pb Crystallization Ages

5.1.1. Group I: Precambrian MTS Basement

[36] The ZUPb ages for the MTS unit (Group I) can be subdivided into three distinct populations. These are interpreted in the context of (1) an intrusion phase associated with Rodina break-up (~850–770 Ma) and (2) Grenvillian (~1200–1000 Ma) and (3) Paleo-Proterozoic (~2500–1850 Ma) crustal recycling events. *Kröner et al.* [2009] dated granitoid gneisses and clastic meta-sediments from the Kyrgyz MTS and obtained similar distinct age components: ~850–760 Ma; ~1160–900 Ma; ~2700–2500 Ma. These ZUPb age patterns, in particular the occurrence of Grenvillian ages, point toward a similarity of the MTS with the Tarim Block (Figure 1). It is thought that during the Neo-Proterozoic (~850–800 Ma), the incipient break-up of Rodinia effectively gave rise to three major continental blocks. Most of these were characterized by passive margins related with the rifting during that time. However, the Rodinian block incorporating the North China, Siberian and Tarim-MTS continents, was bordered by an active margin, giving rise to the intense granitoid intrusive and rhyolitic extrusive magmatism at that time (840–825 Ma) [*Kheraskova et al.*, 2010].

[37] An extensive ZUPb data set on both igneous and detrital rocks with similar age populations exists for the Tarim Block [e.g., *C. L. Zhang et al.*, 2007, 2009; *Shu et al.*, 2011]. These ages are interpreted in the context of supercontinent cycles. Late Neo-Archean–Early Paleo-Proterozoic ages (∼2700–2300 Ma) [*C. L. Zhang et al.*, 2007; *Shu et al.*, 2011] can be linked with world-wide crust formation events [e.g., *Zhao et al.*, 2002]. Late Paleo-Proterozoic ages (∼2000–1800 Ma) refer to the assembly of the Columbia supercontinent [*Zhao et al.*, 2002; *Hou et al.*, 2008; *Shu et al.*, 2011]. Grenvillian (∼1150–900 Ma) and Neo-Proterozoic (∼830–745 Ma) ZUPb ages from Tarim are interpreted in the context of the assembly and break-up of the Rodinia supercontinent respectively [*Zhang et al.*, 2009; *Shu et al.*, 2011].

5.1.2. Group II and Inherited Ages in Group III: Late Caledonian Signals, North of the STSs

[38] The Paleozoic history of the Tien Shan is dominated by the closure of several branches of the PAO. Extensive Caledonian (Cambro-Silurian) magmatism in the NTS can be interpreted in that context, and is related to the closure of the Terskey Ocean and the assembly of Paleo-Kazakhstan [*Konopelko et al.*, 2008; *Glorie et al.*, 2010]. The then newly formed active margin of the Paleo-Kazakhstan continent underwent further growth during Silurian and Devonian northward subduction of the Turkestan oceanic crust [*Konopelko et al.*, 2008]. The occurrence of Late Silurian–Early Devonian intrusions at the southern edge of the MTS (AI-71, 73; 420–405 Ma) can be interpreted in this framework. These ages correspond well with ZUPb data (∼425–400 Ma) obtained for granitoids in the Chinese MTS [*Chen et al.*, 2010; *Ren et al.*, 2011; *Dong et al.*, 2011]. Also one more Early Devonian (∼416 Ma) intrusion was recognized in the Uzbek MTS segment [*Seltmann et al.*, 2011]. These authors suggested that the MTS intrusions formed in a back-arc extensional setting, due to their intraplate position relative to the active Paleo-Kazakhstan margin.

[39] The Turkestan Ocean opened during the Early Ordovician, which implies that the MTS had already been separated from Tarim during that time. This observation is evidenced by the occurrence of Ordovician ophiolites in the STS [*Biske and Seltmann*, 2010, and references therein]. The ZUPb results for tonalite sample AI-60, which intruded the Atbashi ophiolitic tectonic mélange during Hercynian times, indicate inherited Late Cambrian (∼504 Ma) and Silurian (∼429 Ma) concordant components. The ∼428 Ma inherited concordant component for this sample corresponds to the crystallization age (∼436 Ma) of a calc-alkaline gabbro in the Atbashi ophiolitic tectonic mélange [*Kröner et al.*, 2009]. These results bear witness to the aforementioned Silurian–Early Devonian magmatic event related to subduction of the Turkestan Ocean. The presence of this magmatic episode is further underscored by a similar inherited ZUPb age component in the Terektinsky complex (AI-13; ∼440 Ma) (further discussed below). The origin for the older xenocrysts of ∼504 Ma in this sample is unclear. They might have formed during the initial opening of the Turkestan Ocean but without additional information, this hypothesis remains highly speculative.

5.1.3. Group III: Hercynian STSs Formation

[40] The youngest ZUPb age component of sample AI-60 (∼282 Ma) dates the intrustion of the tonalite in the Atbashi ophiolitic mélange and post-dates the final closure of the Turkestan Ocean, and the formation of the STSs. This observation is in good agreement with recent ZUPb data (∼285 Ma) for a granitic dike that crosscuts the Chinese equivalent of the Atbashi metamorphic belt [*Gao et al.*, 2011]. This event effectively post-dates the final closure of the PAO and the final amalgamation of the CAOB. More evidence for the Late Paleozoic closure comes from the Hercynian Terektinsky complex. Our ZUPb data (∼302–288 Ma) for this intrusive complex are in agreement with previously reported Early Permian (295–292 Ma) granitoid crystallization ages [*Konopelko et al.*, 2009]. The occurrence of a Silurian (∼440 Ma) ZUPb age component in our data from the Terektinsky complex is in agreement with the conclusions of *Grishenko* [1985] who recognized a minor Silurian phase (Kaindybulak complex) and argues against the conclusions of *Konopelko et al.* [2008] who found only Early Permian zircons. As described earlier, our results also include a younger age component (∼220 Ma) which can be attributed to hydrothermal activity and does not date the emplacement of the Terektinsky complex. Triassic ZUPb ages were also found in the Chinese (235–220 Ma) [*L. F. Zhang et al.*, 2007; *Gao et al.*, 2011, and references therein] and the Uzbek (∼240–220 Ma) [*Wilde et al.*, 2001; *Morelli et al.*, 2007; *Seltmann et al.*, 2011] STSs segments. In both cases, a similar hydrothermal origin (fluid-mediated recrystallization) was proposed for these zircons [*Wilde et al.*, 2001; *de Jong et al.*, 2009].

[41] South of the STSs, A-type intrusions were dated in this study and yielded Early Permian (∼290–280 Ma) crystallization ages. *Konopelko et al.* [2007, 2009] found an identical narrow ZUPb age interval for some of these plutons. These authors furthermore found somewhat older ages for the Tashkoro (∼299 Ma) intrusive complex, at the southern edge of the STSs. For the latter, we found an even slightly older age of ∼307 Ma. *Konopelko et al.* [2007, 2009] attribute this episode of granitoid magmatism to crustal melting as a result of ascending asthenospheric mantle in the STSs, which had evolved into a post-collisional mega-shear zone at that time. This interpretation again argues for a Pre-Permian closure of the Turkestan Ocean and coeval formation of the STSs. This episode was expressed by extensive Permian strike-slip movements throughout the Tien Shan at the end of Pangean assembly [*Bazhenov et al.*, 1999; *Van der Voo et al.*, 2006].

5.2. STSs Reactivation: Thermochronological Data

5.2.1. Post-Magmatic/-Hydrothermal Cooling and Initiation of Exhumation

[42] After the Late Paleozoic STS orogeny, the Tarim microcontinent was attached to Paleo-Kazakhstan and the STSs was transformed into a large-scale sinistral shear-zone. Strike-slip movements led to the formation of a narrow Early Permian pull-apart basin in the Inylchek segment of the STSs [*Bazhenov et al.*, 1993, 1999]. The accommodation space thus created allowed associated granitoids, such as the Terektinsky complex, to cool rapidly to upper-crustal temperatures, passing the threshold of the TFT closure temperature. This model explains why the Early Permian TFT age (∼282 Ma) of the Terektinsky complex is nearly identical within error to its ZUPb crystallization age (∼302–288 Ma).

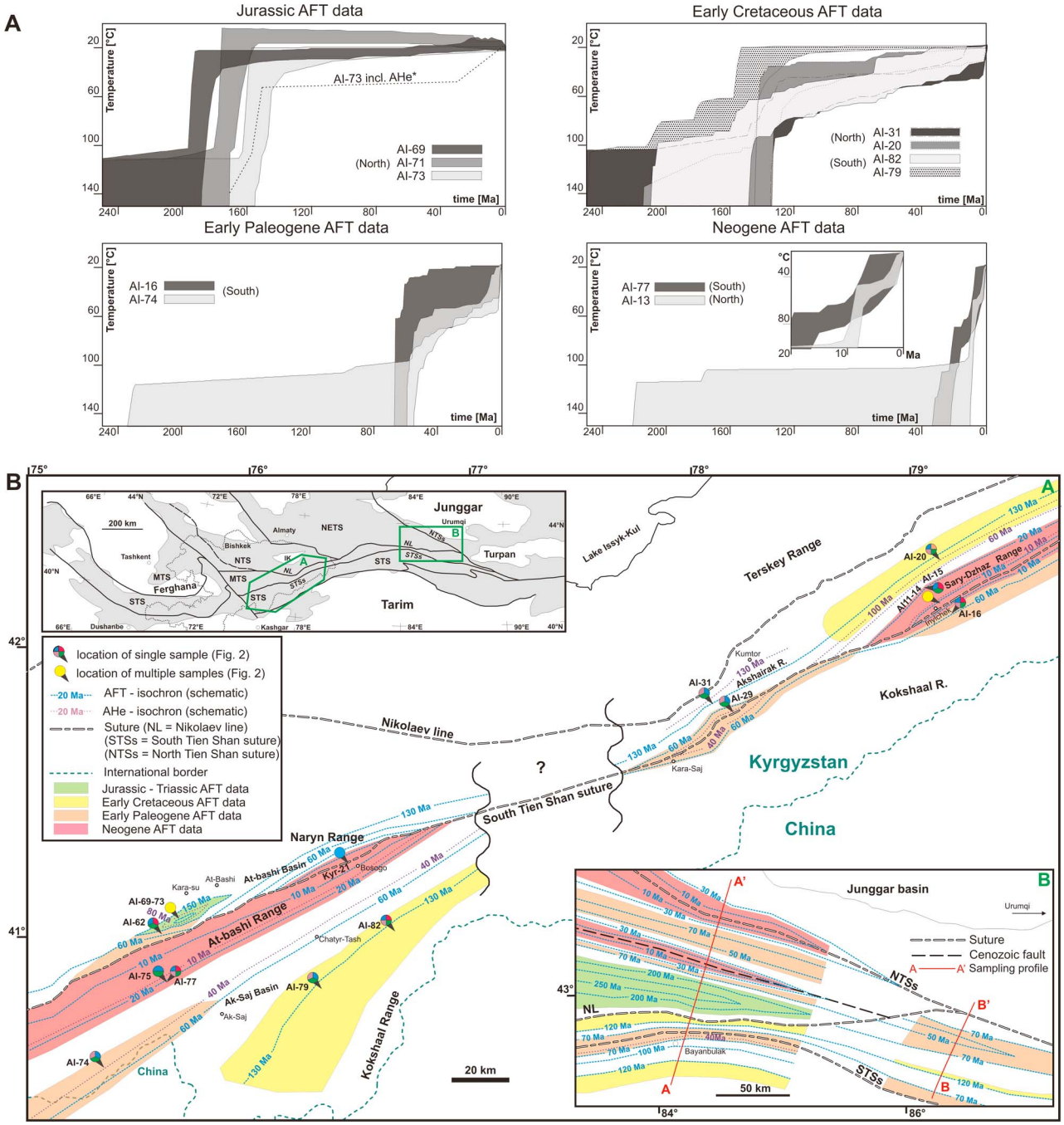

Figure 5. (a) Thermal history models for different areas based on the AFT age and length data and, where possible, AHe age results [*Ketcham*, 2005]. Time-temperature box constraints were placed where ZHe, AFT and AHe ages were available. See text for further details on the modeling strategy. Four groups of thermal histories could be identified. (b) Evaluation of the geographical distribution of our obtained low-temperature thermochronological data with respect to the STSs. Thermal history groups were indicated (colored contours) and isochron lines were drawn as a first order interpretation of the data and as a comparison to available data in the Chinese segment of the STSs [*Dumitru et al.*, 2001; *Q. Wang et al.*, 2009; *Jolivet et al.*, 2010]. Due to the relative low sample site density, some interpolation was necessary and therefore caution is needed when interpreting the isochron maps in too much detail. See text for further discussion.

[43] Another consequence of this transition to a broader extensional tectonic regime is the rapid subsidence of the Tarim basin during the Early–Middle Permian [*Carroll et al.*, 1995]. The basement drop associated with the Tarim subsidence initiated denudation in the flanking STS that remained a topographic high with respect to Tarim. This configuration further explains the occurrence of a Permian (~275–250 Ma) ZHe cooling signal at the northern edge of the STSs. During this time-interval mafic intrusions were emplaced in Tarim that are likely the result of a ~275–270 Ma mantle plume, reflecting the early stages of Pangea break-up [*Pirajno*, 2010; *Zhang et al.*, 2010].

[44] In the Late Permian–Triassic, the STS underwent renewed transpressional deformation, coevally with mainly basaltic volcanic activity at the northern edge of Tarim [*Carroll et al.*, 1995]. This transpressional regime provoked hydrothermal activity [e.g., *Pirajno*, 2010], which could explain the occurrence of Triassic (~230–210 Ma) reset TFT and ZHe ages in parts of the Terektinsky complex. These reset ages correspond to the supposed hydrothermal ZUPb ages and record fast cooling after hot fluids migrated through the intrusives bordering the suture.

5.2.2. Cimmerian Signals

[45] In the Late Paleozoic–Early Mesozoic, the ancestral Tien Shan was a consolidated part of Eurasia. The growth of Eurasia was however far from completed. Its southern margin, south of Tarim, became an active margin during the Mesozoic where Paleo-Tethys oceanic crust was being consumed. During the closure of this oceanic basin, several peri-Gondwanan blocks drifted northward and collided with the Eurasian margin during the punctuated Cimmerian orogeny [*Schwab et al.*, 2004; *De Grave et al.*, 2007; *Kapp et al.*, 2007; *Glorie et al.*, 2010]. As a result of the Cimmerian compressive forces, the Tarim basin subsided further and formed a foreland basin adjacent to the Mesozoic Tien Shan that became uplifted simultaneously [*Allen and Vincent*, 1997; *Sobel et al.*, 2006b; *De Grave et al.*, 2007; *Glorie et al.*, 2010; *Jolivet et al.*, 2010]. As a consequence the Tien Shan basement was subjected to exhumation. This exhumation is responsible for the widespread occurrence of Jurassic-Cretaceous (~190–110 Ma) AFT and AHe ages which are not only limited to the vicinity of the STS suture (Figure 2) but are also found in other locations in the Tien Shan [e.g., *De Grave et al.* 2007; *Glorie et al.* 2010]. The stress-field induced by the Cimmerian collisions at the southern Eurasian margin propagated to the North and in this way reactivated Paleozoic structures such as the STSs in the Tien Shan [*Allen and Vincent*, 1997; *Poupinet et al.*, 2002; *Buslov et al.*, 2007].

[46] First signs of this reactivation episode are well preserved in the Kembel massif granitoid basement (~190–150 Ma), just north of the STSs (Figure 2). If we omit the AHe data, a simple thermochronological model can be derived for the Kembel massif (samples AI-69, 71, 73) which clearly exhibits rapid cooling in the Jurassic (Figure 5a). If we include the AHe data, the HeFTy-program [*Ketcham*, 2005] was not able to return good fit paths due to the discrepancy between the long AFT lengths versus younger AHe ages. In the case that we include the AHe data to the modeling input, statistical acceptable *tT*-paths could still however be obtained and these also show rapid Jurassic cooling until ~50°C, followed by a second cooling step to ambient temperatures, starting at ~30 Ma (Figure 5a, dashed *tT*-path). The timing of the latter increase in cooling rate corresponds to an Early Cenozoic reactivation signal also exhibited by other samples, in close vicinity of the STSs, as will be discussed below.

[47] More widespread, both north and south of the STSs, an Early Cretaceous (~140–110 Ma) cooling phase can be recognized. The modeled *tT*-paths for samples north of the STSs (AI-20, 31) exhibit rapid cooling similar to the Kembel massif. South of the STSs (AI-79, 82), the resulting cooling rate is more gradual (Figure 5a).

[48] This Jurassic-Cretaceous cooling episode for the Tien Shan basement was previously observed in several thermochronological studies in adjoining regions [*Dumitru et al.*, 2001; *Sobel et al.*, 2006b; *De Grave et al.*, 2007; *Glorie et al.*, 2010; *De Grave et al.*, 2011a, 2011b]. Thermal history models in these studies record Mesozoic cooling between generally ~200 Ma and ~110 Ma which corresponds very well to the results presented here.

5.2.3. Early Cenozoic Reactivation

[49] At several locations, more localized in the Kyrgyz STS suture, Early Cenozoic AFT and AHe ages were found. The fact that the Early Paleogene ZHe and AFT ages for the Tashkoro intrusion (AI-16; Figure 2) are equal within error indicates that these ages do not represent mixed ages between older and younger events, but refer to a distinct cooling phase at ~60–45 Ma. The thermal history models for samples AI-16 and AI-74 support this observation (Figure 5a). The secondary cooling peak for sample AI-74 (from ~10 Ma onwards) corresponds to a Neogene reactivation phase, discussed below.

[50] During the Early Paleogene, a large amount of clastic sediments from eroding adjacent mountain ranges were deposited into the intramontane and foreland basins such as the Tarim Basin. *Hendrix et al.* [1992] recognized an increased rate of basin subsidence, coeval with the deposition of alluvial conglomerates in the northern Tarim Basin at ~75–65 Ma. Furthermore in this study, an Early Paleogene (~61 Ma) AFT age component from detrital apatites from the *Kokturpak Formation*, adjacent to the Atbashi Range (Figure 2) was obtained. This further underscores the existence of an Early Paleogene exhumation episode in the Tien Shan. The Early Cretaceous (~124 Ma) detrital AFT signal in the same sample gives more evidence for the previously described Mesozoic reactivation phase. The occurrence of a small amount of older (~241 Ma) grains might correspond to limited influx from the Song-Kul plateau, in the north of our study area [*De Grave et al.*, 2011a] or from other older basement source areas.

[51] Hence, the Early Paleogene cooling phase can be interpreted as an effect of strongly localized denudation of intrusives bordering the STSs. This denudation episode reflects Early Cenozoic reactivation of the STSs as a response to a post-Cimmerian phase of deformation. Similar AFT and AHe ages (~65–55 Ma) were found in the Chinese Tien Shan, at the eastern extension of the STSs [*Dumitru et al.*, 2001; *Q. Wang et al.*, 2009; *Jolivet et al.*, 2010]. The origin for this reactivation episode is still debated. Possibly the Early Paleogene reactivation can be explained as a distant effect of the accretion of the Kohistan-Dras island arc and the Karakoram Block to the southern Meso-Cenozoic Eurasian margin. The assembly of these blocks

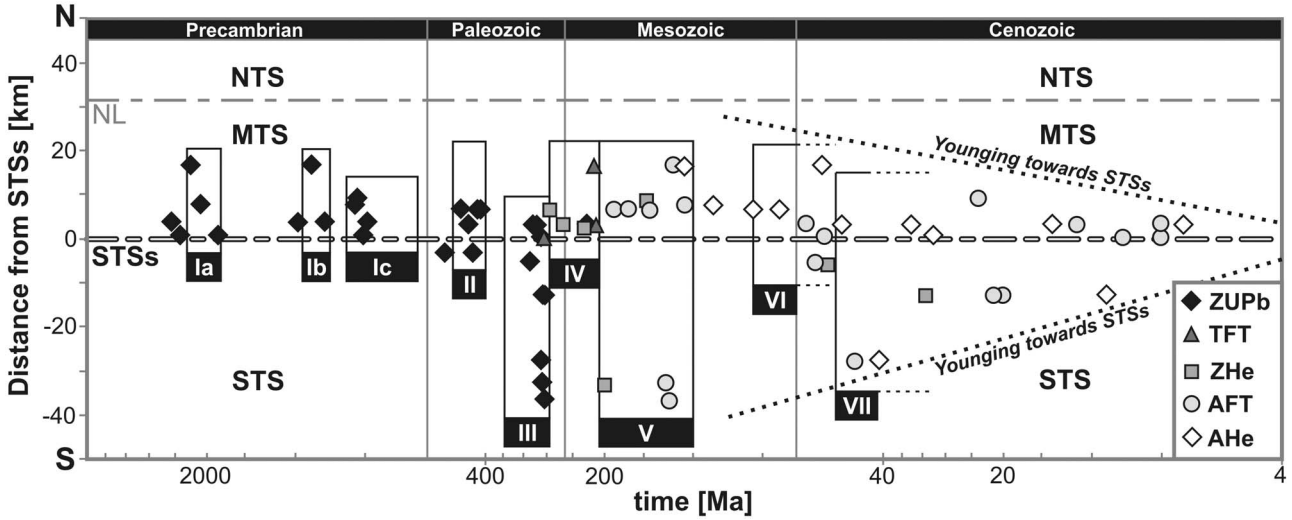

Figure 6. Summary of all obtained ages on a log-*t* scale versus their distance from the STSs. Nine (Ia, Ib, Ic, II, III, IV, V, VI, and VII) age groups were identified which refer to the tectonic events, described in section 6.

induced tectonic activity in the Pamirs and rejuvenation of the Tien Shan [*Hendrix et al.*, 1992; *Schwab et al.*, 2004; *De Grave et al.*, 2007; *Jolivet et al.*, 2010; *De Grave et al.*, 2011a].

[52] *Jolivet et al.* [2010] described an alternative driving mechanism for the Early Paleogene reactivation in the Tien Shan. In their model, the reactivation might also be related with the Cretaceous Mongol-Okhotsk collision of Siberia to the Mongolia-North China Block [e.g., *Lin et al.*, 2008]. It has been shown that this large orogeny induced crustal thickening in Mongolia and probably initiated the Baikal rift in Siberia [*Jolivet et al.*, 2010, and references therein]. Probably both events contributed to the Early Paleogene Tien Shan reactivation. We do however favor the collision of Kohistan-Dras as main actor for the reactivation due to the more proximal position of the collision zone relative to the Kyrgyz Tien Shan.

5.2.4. Neogene Reactivation

[53] Based on geodetic and magnetostratigraphic observations, the onset of the modern Tien Shan mountain building is estimated at ~12–10 Ma [e.g., *Abdrakhmatov et al.*, 1996; *Reigber et al.*, 2001; *Charreau et al.*, 2006]. Previously reported sedimentological and thermochronological data however, indicate that the onset of crustal shortening in the Chinese Tien Shan already started in the Late Oligocene–Early Miocene [*Hendrix et al.*, 1994; *Yin et al.*, 1998; *Bullen et al.*, 2001; *Sobel et al.*, 2006a]. This discrepancy was explained by *Sobel et al.* [2006a], who argued that the shortening rate was not constant through time and intensified at ~10 Ma.

[54] Our ZHe data indicates exhumation at ~30 Ma for the Atbashi Range, just South of the STSs (Figure 2; AI-77). Corresponding AFT ages of ~25–20 Ma were found in both the Atbashi and Sary-Dzhaz Range (Figure 2). The thermal history model for sample AI-77 shows two phases of rapid cooling (1) from ~30 to 18 Ma and (2) from ~10 Ma to present (Figure 5a). The Miocene episode of fast cooling was also found in the thermal history model for the Terektinsky complex (from ~10 to 8 Ma) and is further supported by the Miocene AFT age (~8 Ma) for sample Kyr-21 at the eastern tip of the Atbashi Range (Figure 2). The thermal history model for sample AI-13 (Terektinsky complex) shows a third and even more recent cooling step from ~2 Ma onwards. These results hence corroborate the model described above and explain that the onset of the modern Tien Shan mountain building started in the Late Oligocene (~30–25 Ma) and intensified in the Miocene (~10–8 Ma) and the Pliocene (~3–2 Ma) [*Bullen et al.*, 2001; *Sobel et al.*, 2006a; *De Grave et al.*, 2007; *Glorie et al.*, 2010].

[55] The indentation of the Indian plate into Eurasia is thought to be the driving force for the Late Cenozoic Tien Shan rejuvenation phases [*Yin et al.*, 1998; *Poupinet et al.*, 2002; *Buslov et al.*, 2007; *De Grave et al.*, 2007]. Stress and strain at the India-Eurasia collision zone caused crustal shortening and uplift in the Himalayas and Tibet but also propagated further in the lithosphere through the rigid Tarim Block into the weaker crust of the Pamirs and the Tien Shan, where it invoked deformation [*Avouac et al.*, 1993; *De Grave et al.*, 2007]. Stepwise exhumation/denudation in the Tien Shan is also evident from changes of the sediment accumulation rate in the adjacent Tarim and Junggar basins [*Métivier and Gaudemer*, 1997] and the Tien Shan intramontane basins [*Cobbold et al.*, 1994].

5.2.5. Resulting Low-Temperature Isochron Map for the STSs

[56] The reactivation phases described above show a distinct geographical distribution pattern relative to the STSs, with the youngest, Neogene ages in the suture itself (Figure 5b). In order to shed more light on this distinctive pattern, AFT- and AHe-isochrons were constructed in close vicinity of the STSs (Figure 5b). Due the relative low sample site density, some interpolation was necessary and therefore caution is needed when interpreting the isochron map in too much detail. The main observed trends however are consistent over the entire study area and can be compared with data sets from *Dumitru et al.* [2001], *Q. Wang et al.* [2009], and *Jolivet et al.* [2010] at the eastern extension of the Chinese STSs. In latter study areas, the Tien Shan is characterized by a narrower and more deformed zone squeezed in between

the Junggar and Tarim Blocks. Here several Tien Shan sutures merge and their responses to neotectonic deformation are more influenced by each other, compared to their Kyrgyz counterparts (Figures 1 and 6).

[57] The Atbashi and Inylchek STSs segments clearly show younger AFT and AHe ages toward the axis of the suture, providing evidence for localized Late Cenozoic reactivation in the STSs (Figure 5b). Further away from the suture, first the Early Paleogene and then the Cimmerian ages are found. In the Akshairak region of the STSs, Neogene AFT and AHe ages were not found. In the Chinese Tien Shan, Early Paleogene reactivation is mainly localized around the NTSs, STSs and an intervening Cenozoic thrust fault (Hexilagen fault). Neogene reactivation is absent or hitherto undetected in the Chinese STSs, which was accommodated by the NTSs and the Hexilagen fault, to its north. These observations imply that the timing of fault-induced denudation varies along strike of the STSs. Nonetheless, our thermochronological data gives clear evidence of localized reactivation along the STSs and confirm that inherited basement structures have major control on the reactivation of the ancestral Tien Shan.

6. Conclusions

[58] Our multichronological data set across the Kyrgyz STS suture and its suturing tectonic units is summarized in Figure 6. The resulting ages can be linked to distinct events in the tectonic history of the South Kyrgyz Tien Shan and show the dominant role of the pre-existing basement architecture during intracontinental deformation. It demonstrates that the deformation has not migrated steadily into the forelands, but was focused on pre-existing basement structures.

[59] I. ZUPb data for the Middle Tien Shan (MTS) reveal (Ia) Paleo-Proterozoic (∼2500–1850 Ma), (Ib) Grenvillian (∼1200–1000 Ma) and (Ic) Rodinia break-up (∼850–770 Ma) signals which presumably indicate that the MTS was once part of the Tarim Block. In the Early Paleozoic, both terranes became separated by the Turkestan Ocean, a branch of the Paleo-Asian Ocean.

[60] II. Late Caledonian (∼440–405 Ma) ZUPb ages were found at several locations just north of the Kyrgyz STSs. These correspond to Silurian and Early Devonian magmatic episodes related to subduction of the Turkestan ocean.

[61] III. Hercynian (∼290–280 Ma) ZUPb ages were obtained for granitoid A-type intrusions in the STS. Closer to the STS suture, the Terektinsky and Tashkoro complexes record ∼310–290 Ma ZUPb signals, constraining a minimum age for the final closure of the Turkestan ocean.

[62] IV. Late Permian–Triassic (∼280–210 Ma) TFT and ZHe ages record a first sign of Tien Shan exhumation as a response to subsidence of the Tarim basin. This temporary extensional tectonic phase also may explain the occurrence of presumed hydrothermal activity in the Terektinsky complex.

[63] V. As a response to the punctuated accretion of Cimmerian blocks to the Mesozoic Eurasian margin, a Mesozoic Tien Shan orogen was built. Our results point to a Jurassic (∼190–150 Ma) and an Early Cretaceous (∼140–110 Ma) Cimmerian AFT/AHe signal in both the MTS and STS.

[64] VI. Low-temperature thermochronological results record a renewed period of STSs reactivation in the Early Paleogene (∼60–45 Ma). The driving force for this exhumation phase is still debated, but likely it is a result of the collision of the Kohistan-Dras island arc with Eurasia.

[65] VII. Neogene (∼30–6 Ma) low-temperature cooling ages were obtained for samples, from within the STSs. Thermal history modeling reveals an onset of mountain building in the Late Oligocene (∼30–25 Ma) which intensified in the Miocene (∼10–8 Ma) and the Pliocene (∼3–2 Ma). These signals are interpreted as related to the punctuated indentation of India into Eurasia.

[66] **Acknowledgments.** The authors were supported by grants from the Institute for the Promotion of Innovation through Science and Technology in Flanders (IWT-Vlaanderen) (SG) and the Fund for Scientific Research-Flanders (FWO, Belgium) (JDG). This research was also co-funded by Ghent University (BOF–bilateral project 01SB1309). We are indebted to Guido Vittiglio and Peter Vermaercke for help with irradiations and neutron dosimetry at the Belgian Nuclear Research Centre in Mol (SCK-CEN, BR1 facility). O. Oncken (Editor), M. Allen, and an anonymous reviewer are thanked for their insightful comments which helped to improve this paper.

References

Abdrakhmatov, K. Y., et al. (1996), Relatively recent construction of the Tien Shan inferred from GPS measurements of present-day crustal deformation rates, *Nature*, *384*(6608), 450–453, doi:10.1038/384450a0.

Alekseev, D. V., V. A. Aristov, and K. E. Degtyarev (2007), The age and tectonic setting of volcanic and cherty sequences in the ophiolite complex of the Atbashe Ridge (Southern Tien Shan), *Dokl. Earth Sci.*, *413*(2), 380–383, doi:10.1134/S1028334X07030130.

Alexeiev, D. V., H. E. Cook, V. M. Buvtyshkin, and L. Y. Golub (2009), Structural evoltution of the Ural-Tian Shan junction: A view from Karatau ridge, South Kazakhstan, *C. R. Geosci.*, *341*(2–3), 287–297, doi:10.1016/j.crte.2008.12.004.

Allen, M. B., and S. J. Vincent (1997), Fault reactivation in the Junggar region, northwest China: The role of basement structures during Mesozoic-Cenozoic compression, *J. Geol. Soc.*, *154*, 151–155, doi:10.1144/gsjgs.154.1.0151.

Allen, M. B., B. F. Windley, and Z. Chi (1993), Paleozoic Collisional tectonics and magmatism of the Chinese Tien-Shan, central Asia, *Tectonophysics*, *220*(1–4), 89–115, doi:10.1016/0040-1951(93)90225-9.

Allen, M. B., G. I. Alsop, and V. G. Zhemchuzhnikov (2001), Dome and basin refolding and transpressive inversion along the Karatau Fault System, southern Kazakstan, *J. Geol. Soc.*, *158*, 83–95, doi:10.1144/jgs.158.1.83.

Avouac, J. P., P. Tapponnier, M. Bai, H. You, and G. Wang (1993), Active thrusting and folding along the Northern Tien-Shan and Late Cenozoic rotation of the Tarim relative to Dzungaria and Kazakhstan, *J. Geophys. Res.*, *98*(B4), 6755–6804, doi:10.1029/92JB01963.

Bazhenov, M. L., A. Chauvin, M. Audibert, and N. M. Levashova (1993), Permian and Triassic paleomagnetism of the southwestern Tien Shan: Timing and mode of tectonic rotations, *Earth Planet. Sci. Lett.*, *118*(1–4), 195–212, doi:10.1016/0012-821X(93)90168-9.

Bazhenov, M. L., V. S. Burtman, and A. V. Dvorova (1999), Permian paleomagnetism of the Tien Shan fold belt, Central Asia: Post-collisional rotations and deformation, *Tectonophysics*, *312*(2–4), 303–329, doi:10.1016/S0040-1951(99)00181-X.

Biske, Y. S., and R. Seltmann (2010), Paleozoic Tian-Shan as a transitional region between the Rheic and Urals-Turkestan oceans, *Gondwana Res.*, *17*(2–3), 602–613, doi:10.1016/j.gr.2009.11.014.

Bullen, M. E., D. W. Burbank, J. I. Garver, and K. Y. Abdrakhmatov (2001), Late Cenozoic tectonic evolution of the northwestern Tien Shan: New age estimates for the initiation of mountain building, *Geol. Soc. Am. Bull.*, *113*(12), 1544–1559, doi:10.1130/0016-7606(2001)113<1544:LCTEOT>2.0.CO;2.

Burtman, V. S., S. F. Skobelev, and P. Molnar (1996), Late Cenozoic slip on the Talas-Ferghana fault, the Tien Shan, central Asia, *Geol. Soc. Am. Bull.*, *108*(8), 1004–1021, doi:10.1130/0016-7606(1996)108<1004:LCSOTT>2.3.CO;2.

Buslov, M. M., J. De Grave, E. A. V. Bataleva, and V. Y. Batalev (2007), Cenozoic tectonic and geodynamic evolution of the Kyrgyz Tien Shan Mountains: A review of geological, thermochronological and geophysical data, *J. Asian Earth Sci.*, *29*(2–3), 205–214, doi:10.1016/j.jseaes.2006.07.001.

Carroll, A. R., S. A. Graham, M. S. Hendrix, D. Ying, and D. Zhou (1995), Late Paleozoic Tectonic Amalgamation of Northwestern China–Sedimentary

Record of the Northern Tarim, Northwestern Turpan, and Southern Junggar Basins, *Geol. Soc. Am. Bull.*, *107*(5), 571–594, doi:10.1130/0016-7606(1995)107<0571:LPTAON>2.3.CO;2.

Charreau, J., S. Gilder, Y. Chen, S. Dominguez, J. P. Avouac, S. Sen, M. Jolivet, Y. G. Li, and W. M. Wang (2006), Magnetostratigraphy of the Yaha section, Tarim Basin (China): 11 Ma acceleration in erosion and uplift of the Tian Shan mountains, *Geology*, *34*(3), 181–184, doi:10.1130/G22106.1.

Chen, J. F., B. F. Han, J. Q. Ji, L. Zhang, Z. Xu, G. Q. He, and T. Wang (2010), Zircon U-Pb ages and tectonic implications of Paleozoic plutons in northern West Junggar, North Xinjiang, China, *Lithos*, *115*(1–4), 137–152, doi:10.1016/j.lithos.2009.11.014.

Cherniak, D., and E. Watson (2003), Diffusion in zircon, in *Zircon*, *Rev. Mineral. Geochem.*, vol. 53, edited by J. Hanchar and P. Hoskin, pp. 113–139, Mineral. Soc. of Am., Washington, D. C.

Cobbold, P. R., E. Sadybakasov, and J. C. Thomas (1994), Cenozoic transpression and basin development, Kyrghyz Tienshan, Central Asia, in *Geodynamic Evolution of Sedimentary Basins*, edited by F. Roure et al., pp. 181–202, Ed. Technip, Paris.

De Grave, J., M. M. Buslov, and P. Van den haute (2007), Distant effects of India-Eurasia convergence and Mesozoic intracontinental deformation in Central Asia: Constraints from apatite fission-track thermochronology, *J. Asian Earth Sci.*, *29*(2–3), 188–204, doi:10.1016/j.jseaes.2006.03.001.

De Grave, J., S. Glorie, M. M. Buslov, A. Izmer, A. Fournier-Carrie, V. Y. Batalev, F. Vanhaecke, M. A. Elburg, and P. Van den haute (2011a), The thermo-tectonic history of the Song-Kul Plateau, Kyrgyz Tien Shan: Constraints by apatite and titanite thermochronometry and zircon U/Pb dating, *Gondwana Res.*, *20*, 745–763, doi:10.1016/j.gr.2011.03.011.

De Grave, J., S. Glorie, A. Ryabinin, F. Zhimulev, M. M. Buslov, A. Izmer, M. Elburg, F. Vanhaecke, and P. Van den haute (2011b), Late Palaeozoic and Meso-Cenozoic tectonic evolution of the Southern Kyrgyz Tien Shan: Constraints from multi-method thermochronology in the Trans-Alai, Turkestan-Alai Section and the Southeastern Ferghana Basin, *J. Asian Earth Sci.*, doi:10.1016/j.jseaes.2011.04.019, in press.

de Jong, K., B. Wang, M. Faure, L. S. Shu, D. Cluzel, J. Charvet, G. Ruffet, and Y. Chen (2009), New Ar^{40}/Ar^{39} age constraints on the Late Palaeozoic tectonic evolution of the western Tianshan (Xinjiang, northwestern China), with emphasis on Permian fluid ingress, *Int. J. Earth Sci.*, *98*(6), 1239–1258, doi:10.1007/s00531-008-0338-8.

Donelick, R. A., R. A. Ketcham, and W. D. Carlson (1999), Variability of apatite fission-track annealing kinetics: II. Crystallographic orientation effects, *Am. Mineral.*, *84*(9), 1224–1234.

Dong, Y., G. Zhang, F. Neubauer, X. Liu, C. Hauzenberger, D. Zhou, and W. Li (2011), Syn- and post-collisional granitoids in the Central Tianshan orogen: Geochemistry, geochronology and implications for tectonic evolution, *Gondwana Res.*, *20*, 568–581, doi:10.1016/j.gr.2011.01.013.

Dumitru, T. A., D. Zhou, E. Z. Chang, and S. A. Graham (2001), Uplift, exhumation, and deformation in the Chinese Tien Shan, in *Paleozoic and Mesozoic Tectonic Evolution of Central Asia: From Continental Assembly to Intracontinental Deformation*, edited by M. S. Hendrix and G. A. Davis, *Mem. Geol. Soc. Am.*, *194*, 71–99, doi:10.1130/0-8137-1194-0.71.

Dunkl, I., T. Mikes, D. Frei, A. Gerdes, and H. von Eynatten (2009), PepiAGE: Data reduction program for time-resolved U/Pb analyses: Introduction and call for tests and discussion, report, 15 pp., Univ. of Goettingen, Copenhagen. [Available at http://www.sediment.uni-goettingen.de/staff/dunkl/zips/PepiAGE-introduction-c1.pdf.]

Ehlers, T. A., and K. A. Farley (2003), Apatite (U-Th)/He thermochronometry: Methods and applications to problems in tectonic and surface processes, *Earth Planet. Sci. Lett.*, *206*(1–2), 1–14, doi:10.1016/S0012-821X(02)01069-5.

Gao, J., and R. Klemd (2003), Formation of HP-LT rocks and their tectonic implications in the western Tianshan Orogen, NW China: Geochemical and age constraints, *Lithos*, *66*(1–2), 1–22, doi:10.1016/S0024-4937(02)00153-6.

Gao, J., M. S. Li, X. C. Xiao, Y. Q. Tang, and G. Q. He (1998), Paleozoic tectonic evolution of the Tianshan Orogen, northwestern China, *Tectonophysics*, *287*(1–4), 213–231, doi:10.1016/S0040-1951(97)00211-4.

Gao, J., L. L. Long, R. Klemd, Q. Qian, D. Y. Liu, X. M. Xiong, W. Su, W. Liu, Y. T. Wang, and F. Q. Yang (2009), Tectonic evolution of the South Tianshan orogen and adjacent regions, NW China: Geochemical and age constraints of granitoid rocks, *Int. J. Earth Sci.*, *98*(6), 1221–1238, doi:10.1007/s00531-008-0370-8.

Gao, J., R. Klemd, Q. Qian, X. Zhang, J. Li, T. Jiang, and Y. Yang (2011), The collision between the Yili and Tarim blocks of the Southwestern Altaids: Geochemical and age constraints of a leucogranite dike crosscutting the HP-LT metamorphic belt in the Chinese Tianshan Orogen, *Tectonophysics*, *499*, 118–131, doi:10.1016/j.tecto.2011.01.001.

Glorie, S., J. De Grave, M. M. Buslov, M. A. Elburg, D. F. Stockli, A. Gerdes, and P. Van den haute (2010), Multi-method chronometric constraints on the evolution of the Northern Kyrgyz Tien Shan granitoids (Central Asian Orogenic Belt): From emplacement to exhumation, *J. Asian Earth Sci.*, *38*(3–4), 131–146, doi:10.1016/j.jseaes.2009.12.009.

Glorie, S., J. De Grave, M. M. Buslov, F. I. Zhimulev, A. Izmer, W. Vandoorne, A. Ryabinin, P. Van den haute, F. Vanhaecke, and M. A. Elburg (2011), Formation and Palaeozoic evolution of the Gorny-Altai–Altai-Mongolia suture zone (South Siberia): Zircon U/Pb constraints on the igneous record, *Gondwana Res.*, *20*(2–3), 465–484, doi:10.1016/j.gr.2011.03.003.

Green, P. F., P. V. Crowhurst, I. R. Duddy, T. Japsen, and S. P. Holford (2006), Conflicting (U-Th)/He and fission track ages in apatite: Enhanced He retention, not anomalous annealing behaviour, *Earth Planet. Sci. Lett.*, *250*(3–4), 407–427, doi:10.1016/j.epsl.2006.08.022.

Grishenko, V. A. (1985), Geological survey at a scale 1:50 000 within the Saryjaz area: Final report of the Ottuk Department on researches carried out in 1980–1985 [in Russian], report, Arch. of the State Geol. Agency of the Kyrgyz Repub., Frunze, U.S.S.R.

Hegner, E., R. Klemd, A. Kröner, M. Corsini, D. V. Alexeiev, L. M. Iaccheri, T. Zack, P. Dulski, X. Xia, and B. F. Windley (2010), Mineral ages and P-T conditions of Late Paleozoic high-pressure eclogite and provenance of mélange sediments from Atbashi in the south Tianshan orogen of Kyrgyzstan, *Am. J. Sci.*, *310*, 916–950, doi:10.2475/09.2010.07.

Hendrix, M. S., and G. A. Davis (Eds.) (2001), *Paleozoic and Mesozoic Tectonic Evolution of Central Asia: From Continental Assembly to Intracontinental Deformation*, *Mem. Geol. Soc. Am*, vol. 194, 447 pp., Geol. Soc. of Am., Boulder, Colo.

Hendrix, M. S., S. A. Graham, A. R. Carroll, E. R. Sobel, C. L. McKnight, B. J. Shulein, and Z. Wang (1992), Sedimentary record and climtic implications of recurrent deformation in the Tian Shan: Evidence from Mesozoic strata of the north Tarim, south Junggar, and Turpan basins, northwest China, *Geol. Soc. Am. Bull.*, *104*, 53–79, doi:10.1130/0016-7606(1992)104<0053:SRACIO>2.3.CO;2.

Hendrix, M. S., T. A. Dumitru, and S. A. Graham (1994), Late Oligocene–early Miocene unroofing in the Chinese Tien-Shan: An early effect of the India-Asia collision, *Geology*, *22*(6), 487–490, doi:10.1130/0091-7613(1994)022<0487:LOEMUI>2.3.CO;2.

Hoskin, P. W. O., and U. Schaltegger (2003), The composition of zircon and igneous and metamorphic petrogenesis, in *Zircons*, *Rev. Min. Geochem.*, vol. 53, edited by J. M. Hanchar and P. W. O. Hoskin, pp. 27–62, Mineral. Soc. of Am., Washington, D. C., doi:10.2113/0530027.

Hou, G. T., M. Santosh, X. L. Qian, G. S. Lister, and J. H. Li (2008), Configuration of the Late Paleoproterozoic supercontinent Columbia: Insights from radiating mafic dyke swarms, *Gondwana Res.*, *14*(3), 395–409, doi:10.1016/j.gr.2008.01.010.

Jackson, S. E., N. J. Pearson, W. L. Griffin, and E. A. Belousova (2004), The application of laser ablation-inductively coupled plasma-mass spectrometry to in situ U-Pb zircon geochronology, *Chem. Geol.*, *211*(1–2), 47–69, doi:10.1016/j.chemgeo.2004.06.017.

Jacobs, J., and R. J. Thomas (2001), A titanite fission track profile across the southeastern Archaean Kaapvaal Craton and the Mesoproterozoic Natal Metamorphic Province, South Africa: Evidence for differential cryptic meso- to neoproterozoic tectonism, *J. Afr. Earth Sci.*, *33*(2), 323–333, doi:10.1016/S0899-5362(01)80066-X.

Jahn, B. M. (2004), The central Asian orogenic belt and growth of the continental crust in the Phanerozoic, in *Aspects of the Tectonic Evolution of China*, edited by J. Malpas et al., *Geol. Soc. Spec. Publ.*, *226*, 73–100, doi:10.1144/GSL.SP.2004.226.01.05.

Jolivet, M., S. Dominguez, J. Charreau, Y. Chen, Y. G. Li, and Q. C. Wang (2010), Mesozoic and Cenozoic tectonic history of the central Chinese Tian Shan: Reactivated tectonic structures and active deformation, *Tectonics*, *29*, TC6019, doi:10.1029/2010TC002712.

Jonckheere, R., E. Enkelmann, M. Min, C. Trautmann, and L. Ratschbacher (2007), Confined fission tracks in ion-irradiated and step-etched prismatic sections of Durango apatite, *Chem. Geol.*, *242*(1–2), 202–217, doi:10.1016/j.chemgeo.2007.03.015.

Kapp, P., P. G. DeCelles, G. E. Gehrels, M. Heizier, and L. Ding (2007), Geological records of the Lhasa-Qiangtang and Indo-Asian collisions in the Nima area of central Tibet, *Geol. Soc. Am. Bull.*, *119*(7–8), 917–933, doi:10.1130/B26033.1.

Ketcham, R. A. (2005), Forward and inverse modelling of low-temperature thermochronometry data, *Rev. Mineral. Geochem.*, *58*, 275–314, doi:10.2138/rmg.2005.58.11.

Kheraskova, T. N., V. A. Bush, A. N. Didenko, and S. G. Samygin (2010), Breakup of Rodinia and early stages of evolution of the Paleoasian ocean, *Geotectonics, Engl. Transl.*, *44*(1), 3–24, doi:10.1134/S0016852110010024.

Klemd, R., M. Brocker, B. R. Hacker, J. Gao, P. Gans, and K. Wemmer (2005), New age constraints on the metamorphic evolution of the high-

pressure/low-temperature belt in the western Tianshan mountains, NW China, *J. Geol.*, *113*(2), 157–168, doi:10.1086/427666.

Kohn, B. P., M. E. Wagner, T. M. Lutz, and G. Organist (1993), Anomalous Mesozoic thermal regime, central Appalachian-Piedmont: Evidence from sphene and zircon fission-track dating, *J. Geol.*, *101*(6), 779–794, doi:10.1086/648274.

Konopelko, D., G. Biske, R. Seltmann, O. Eklund, and B. Belyatsky (2007), Hercynian post-collisional A-type granites of the Kokshaal Range, Southern Tien Shan, Kyrgyzstan, *Lithos*, *97*(1–2), 140–160, doi:10.1016/j.lithos.2006.12.005.

Konopelko, D., G. Biske, R. Seltmann, M. Kiseleva, D. Matukov, and S. Sergeev (2008), Deciphering Caledonian events: Timing and geochemistry of the Caledonian magmatic arc in the Kyrgyz Tien Shan, *J. Asian Earth Sci.*, *32*(2–4), 131–141, doi:10.1016/j.jseaes.2007.10.017.

Konopelko, D., R. Seltmann, G. Biske, E. Lepekhina, and S. Sergeev (2009), Possible source dichotomy of contemporaneous post-collisional barren I-type versus tin-bearing A-type granites, lying on opposite sides of the South Tien Shan suture, *Ore Geol. Rev.*, *35*(2), 206–216, doi:10.1016/j.oregeorev.2009.01.002.

Kröner, A., D. V. Alexeiev, A. Mikolaichuk, X. Xia, T. Zack, B. F. Windley, M. Sun, Y. Rojas-Agramonte, and D. Liu (2009), New single zircon ages of Precambrian and Palaeozoic rocks from the Northern, Middle and Southern Tianshan belts in Kyrgyzstan, paper presented at International Field Excursion and Workshop on Tectonic Evolution and Crustal Structure of the Tien Shan Belt and Related Terrains in the Central Asian Orogenic Belt, Cent. Asian Inst. of Appl. Geosci., Bishkek, 8–17 June.

Lin, W., M. Faure, S. Nomade, Q. H. Shang, and P. R. Renne (2008), Permian-Triassic amalgamation of Asia: Insights from Northeast China sutures and their place in the final collision of North China and Siberia, *C. R. Geosci.*, *340*(2–3), 190–201, doi:10.1016/j.crte.2007.10.008.

Ludwig, K. (2003), User's manual for Isoplot 3.00: A geochronological toolkit for Microsoft Excel, *Spec. Publ. 4*, Berkeley Geochronol. Cent., Berkeley, Calif.

Métivier, F., and Y. Gaudemer (1997), Mass transfer between eastern Tien Shan and adjacent basins (central Asia): Constraints on regional tectonics and topography, *Geophys. J. Int.*, *128*(1), 1–17, doi:10.1111/j.1365-246X.1997.tb04068.x.

Molnar, P., and P. Tapponnier (1975), Cenozoic tectonics of Asia: Effects of a continental collision, *Science*, *189*(4201), 419–426, doi:10.1126/science.189.4201.419.

Morelli, R., R. A. Creaser, R. Seltmann, F. M. Stuart, D. Selby, and T. Graupner (2007), Age and source constraints for the giant Muruntau gold deposit, Uzbekistan, from coupled Re-Os-He isotopes in arsenopyrite, *Geology*, *35*(9), 795–798, doi:10.1130/G23521A.1.

Pirajno, F. (2010), Intracontinental strike-slip faults, associated magmatism, mineral systems and mantle dynamics: Examples from NW China and Altay-Sayan (Siberia), *J. Geodyn.*, *50*(3–4), 325–346, doi:10.1016/j.jog.2010.01.018.

Poupinet, G., et al. (2002), Intracontinental subduction and Palaeozoic inheritance of the lithosphere suggested by a teleseismic experiment across the Chinese Tien Shan, *Terra Nova*, *14*(1), 18–24, doi:10.1046/j.1365-3121.2002.00391.x.

Qian, Q., J. Gao, R. Klemd, G. Q. He, B. A. Song, D. Y. Liu, and R. H. Xu (2009), Early Paleozoic tectonic evolution of the Chinese South Tianshan Orogen: Constraints from SHRIMP zircon U-Pb geochronology and geochemistry of basaltic and dioritic rocks from Xiate, NW China, *Int. J. Earth Sci.*, *98*(3), 551–569, doi:10.1007/s00531-007-0268-x.

Reigber, C., G. W. Michel, R. Galas, D. Angermann, J. Klotz, J. Y. Chen, A. Papschev, R. Arslanov, V. E. Tzurkov, and M. C. Ishanov (2001), New space geodetic constraints on the distribution of deformation in Central Asia, *Earth Planet. Sci. Lett.*, *191*(1–2), 157–165, doi:10.1016/S0012-821X(01)00414-9.

Reiners, P. W., T. L. Spell, S. Nicolescu, and K. A. Zanetti (2004), Zircon (U-Th)/He thermochronometry: He diffusion and comparisons with Ar-40/Ar-39 dating, *Geochim. Cosmochim. Acta*, *68*(8), 1857–1887, doi:10.1016/j.gca.2003.10.021.

Ren, R., B. F. Han, J. Q. Ji, L. Zhang, Z. Xu, and L. Su (2011), U-Pb age of detrital zircons from the Tekes River, Xinjiang, China, and implications for tectonomagmatic evolution of the South Tian Shan Orogen, *Gondwana Res.*, *19*(2), 460–470, doi:10.1016/j.gr.2010.07.005.

Schwab, M., et al. (2004), Assembly of the Pamirs: Age and origin of magmatic belts from the southern Tien Shan to the southern Pamirs and their relation to Tibet, *Tectonics*, *23*(4), TC4002, doi:10.1029/2003TC001583.

Seltmann, R., D. Konopelko, G. Biske, F. Divaev, and S. Serge (2011), Hercynian post-collisional magmatism in the context of Paleozoic magmatic evolution of the Tien Shan orogenic belt, *J. Asian Earth Sci.*, *42*, 821–838, doi:10.1016/j.jseaes.2010.08.016.

Şengör, A. M. C., B. A. Natalin, and V. S. Burtman (1993), Evolution of the Altaid tectonic collage and Paleozoic crustal growth in Eurasia, *Nature*, *364*, 299–307, doi:10.1038/364299a0.

Shu, L. S., X. L. Deng, W. B. Zhu, D. S. Ma, and W. J. Xiao (2011), Precambrian tectonic evolution of the Tarim Block, NW China: New geochronological insights from the Quruqtagh domain, *J. Asian Earth Sci.*, *42*, 774–790, doi:10.1016/j.jseaes.2010.08.018, in press.

Simonov, V. A., K. S. Sakiev, N. I. Volkova, S. I. Stupakov, and A. V. Travin (2008), Conditions of formation of the Atbashi Ridge eclogites (South Tien Shan), *Russ. Geol. Geophys.*, *49*(11), 803–815, doi:10.1016/j.rgg.2008.04.001.

Sláma, J., et al. (2008), Plesovice zircon–A new natural reference material for U-Pb and Hf isotopic microanalysis, *Chem. Geol.*, *249*(1–2), 1–35, doi:10.1016/j.chemgeo.2007.11.005.

Sobel, E. R., J. Chen, and R. V. Heermance (2006a), Late Oligocene-Early Miocene initiation of shortening in the Southwestern Chinese Tian Shan: Implications for Neogene shortening rate variations, *Earth Planet. Sci. Lett.*, *247*(1–2), 70–81, doi:10.1016/j.epsl.2006.03.048.

Sobel, E. R., M. Oskin, D. Burbank, and A. Mikolaichuk (2006b), Exhumation of basement-cored uplifts: Example of the Kyrgyz Range quantified with apatite fission track thermochronology, *Tectonics*, *25*, TC2008, doi:10.1029/2005TC001809.

Solomovich, L. I. (2007), Postcollisional magmatism in the South Tien Shan Variscan Orogenic Belt, Kyrgyzstan: Evidence for high-temperature and high-pressure collision, *J. Asian Earth Sci.*, *30*(1), 142–153, doi:10.1016/j.jseaes.2006.08.003.

Stockli, D. F., K. A. Farley, and T. A. Dumitru (2000), Calibration of the apatite (U-Th)/He thermochronometer on an exhumed fault block, White Mountains, *Calif. Geol.*, *28*(11), 983–986.

Su, W., J. Gao, R. Klemd, J. L. Li, X. Zhang, X. H. Li, N. S. Chen, and L. Zhang (2010), U-Pb zircon geochronology of Tianshan eclogites in NW China: Implication for the collision between the Yili and Tarim blocks of the southwestern Altaids, *Eur. J. Mineral.*, *22*(4), 473–478, doi:10.1127/0935-1221/2010/0022-2040.

Van der Voo, R., N. M. Levashova, L. I. Skrinnik, T. V. Kara, and M. L. Bazhenov (2006), Late orogenic, large-scale rotations in the Tien Shan and adjacent mobile belts in Kyrgyzstan and Kazakhstan, *Tectonophysics*, *426*(3–4), 335–360, doi:10.1016/j.tecto.2006.08.008.

Vermeesch, P. (2009), RadialPlotter: A Java application for fission track, luminescence and other radial plots, *Radiat. Meas.*, *44*(4), 409–410, doi:10.1016/j.radmeas.2009.05.003.

Wagner, G. A., and P. Van den haute (1992), *Fission Track-Dating*, 258 pp., Kluwer Acad., Dordrecht, Netherlands.

Wang, B., D. Cluzel, L. S. Shu, M. Faure, J. Charvet, Y. Chen, S. Meffre, and K. de Jong (2009), Evolution of calc-alkaline to alkaline magmatism through Carboniferous convergence to Permian transcurrent tectonics, western Chinese Tianshan, *Int. J. Earth Sci.*, *98*(6), 1275–1298, doi:10.1007/s00531-008-0408-y.

Wang, B., M. Faure, L. S. Shu, K. de Jong, J. Charvet, D. Cluzel, B. M. Jahn, Y. Chen, and G. Ruffet (2010), Structural and geochronological study of high-pressure metamorphic rocks in the Kekesu Section (northwestern China): Implications for the Late Paleozoic Tectonics of the Southern Tianshan, *J. Geol.*, *118*(1), 59–77, doi:10.1086/648531.

Wang, Q. C., S. J. Li, and Z. L. Du (2009), Differential uplift of the Chinese Tianshan since the Cretaceous: Constraints from sedimentary petrography and apatite fission-track dating, *Int. J. Earth Sci.*, *98*(6), 1341–1363, doi:10.1007/s00531-009-0436-2.

Wilde, A. R., P. Layer, T. Mernagh, and J. Foster (2001), The giant Muruntau gold deposit geologic, geochronologic, and fluid inclusion constraints on ore genesis, *Econ. Geol.*, *96*(3), 633–644, doi:10.2113/96.3.633.

Windley, B. F., D. Alexeiev, W. J. Xiao, A. Kroner, and G. Badarch (2007), Tectonic models for accretion of the Central Asian Orogenic Belt, *J. Geol. Soc.*, *164*, 31–47, doi:10.1144/0016-76492006-022.

Wolfe, M. R., and D. F. Stockli (2010), Zircon (U-Th)/He thermochronometry in the KTB drill hole, Germany, and its implications for bulk He diffusion kinetics in zircon, *Earth Planet. Sci. Lett.*, *295*(1–2), 69–82, doi:10.1016/j.epsl.2010.03.025.

Xiao, W. J., B. C. Huang, C. M. Han, S. Sun, and J. L. Li (2010), A review of the western part of the Altaids: A key to understanding the architecture of accretionary orogens, *Gondwana Res.*, *18*(2–3), 253–273, doi:10.1016/j.gr.2010.01.007.

Yin, A. (2010), Cenozoic tectonic evolution of Asia: A preliminary synthesis, *Tectonophysics*, *488*(1–4), 293–325, doi:10.1016/j.tecto.2009.06.002.

Yin, A., S. Nie, P. Craig, T. M. Harrison, F. J. Ryerson, X. L. Qian, and G. Yang (1998), Late Cenozoic tectonic evolution of the southern Chinese Tian Shan, *Tectonics*, *17*(1), 1–27, doi:10.1029/97TC03140.

Zhang, C. L., Z. X. Li, X. H. Li, H. F. Yu, and H. M. Ye (2007), An early Paleoproterozoic high-K intrusive complex in southwestern Tarim block,

NW China: Age, geochemistry, and tectonic implications, *Gondwana Res.*, *12*(1–2), 101–112, doi:10.1016/j.gr.2006.10.006.

Zhang, C. L., Z. X. Li, X. H. Li, and H. M. Ye (2009), Neoproterozoic mafic dyke swarms at the northern margin of the Tarim Block, NW China: Age, geochemistry, petrogenesis and tectonic implications, *J. Asian Earth Sci.*, *35*(2), 167–179, doi:10.1016/j.jseaes.2009.02.003.

Zhang, C. L., Z. X. Li, X. H. Li, Y. G. Xu, G. Zhou, and H. M. Ye (2010), A Permian large igneous province in Tarim and Central Asian orogenic belt, NW China: Results of a ca. 275 Ma mantle plume?, *Geol. Soc. Am. Bull.*, *122*(11–12), 2020–2040, doi:10.1130/B30007.1.

Zhang, L. F., Y. L. Ai, X. P. Li, D. Rubatto, B. Song, S. Williams, S. G. Song, D. Ellis, and J. G. Liou (2007), Triassic collision of western Tianshan orogenic belt, China: Evidence from SHRIMP U-Pb dating of zircon from HP/UHP eclogitic rocks, *Lithos*, *96*(1–2), 266–280, doi:10.1016/j.lithos.2006.09.012.

Zhang, Y. Y., S. W. Dong, B. S. Ujkenov, A. K. Mazurov, S. Y. Kim, B. C. Kim, O. Chuluun, O. Tomurtogoo, A. Morozov, and O. Petrov (2004), Geological map 1:2,500,000, in *Atlas of Geological Maps of Central Asia and Adjacent Areas 2002–2007*, edited by T. Li et al., Geol. Publ. House, Beijing.

Zhao, G. C., M. Sun, and S. A. Wilde (2002), Reconstruction of a pre-Rodinia supercontinent: New advances and perspectives, *Chin. Sci. Bull.*, *47*(19), 1585–1588, doi:10.1360/02tb9348.

Zhukov, Y. B., I. Zaharov, L. A. Berezanskii, and P. M. Izranleva (2008), Geological map of the Kyrgyz Republic, scale 1:500.000, Agency of Geol. and Mineral. Resour. of the Kyrgyz Repub., Bishkek, Kyrgystan.

Zonenshain, L. P., M. I. Kuzmin, L. M. Natapov, and B. M. Page (Eds.) (1990), *Geology of the USSR: A Plate-Tectonic Synthesis*, *Geodyn. Ser.*, vol. 21, 242 pp., AGU, Washington, D. C.

V. Y. Batalev, International Geodynamics Research Centre, 720049 Bishkek, Kyrgyzstan.

M. M. Buslov and F. I. Zhimulev, Institute of Geology and Mineralogy, Siberian Branch of the Russian Academy of Sciences, 3 Prosp. Akad. Koptyuga, 630090 Novosibirsk, Russia.

J. De Grave, M. A. Elburg, S. Glorie, and P. Van den haute, Department of Geology and Soil Science, Ghent University, 281-S8 Krijgslaan, B-9000 Ghent, Belgium. (stijn.glorie@ugent.be)

A. Izmer, Department of Analytical Chemistry, Ghent University, 281-S12 Krijgslaan, B-9000 Ghent, Belgium.

D. F. Stockli, Department of Geology, University of Kansas, 1475 Jayhawk Blvd., Lawrence, KS 66045, USA.